MULTI-SENSOR INERTIAL MEASUREMENT SYSTEM FOR ANALYSIS OF SPORTS MOTION

by

Minmin Zhang

B.S. in Mechanical Engineering, Shanghai Jiao Tong University, China, 2007

M.S. in Mechanical Engineering, Shanghai Jiao Tong University, China, 2010

Submitted to the Graduate Faculty of

Swanson School of Engineering in partial fulfillment

of the requirements for the degree of

PhD in Mechanical Engineering

University of Pittsburgh

2014

UNIVERSITY OF PITTSBURGH

SWANSON SCHOOL OF ENGINEERING

This dissertation was presented

by

Minmin Zhang

It was defended on

July 21, 2014

and approved by

Daniel G. Cole, Ph.D., Associate Professor
Department of Mechanical Engineering and Materials Science

Nitin Sharma, Ph.D., Assistant Professor
Department of Mechanical Engineering and Materials Science

Zhi-Hong Mao, Ph.D., Associate Professor
Department of Electrical and Computer Engineering

Dissertation Director: William W. Clark, Ph.D., Professor
Department of Mechanical Engineering and Materials Science

MULTI-SENSOR INERTIAL MEASUREMENT SYSTEM FOR ANALYSIS OF SPORTS MOTION

Minmin Zhang, PhD

University of Pittsburgh, 2014

A portable motion analysis system that can accurately measure body movement kinematics and kinetics has the potential to benefit athletes and coaches in performance improvement and injury prevention. In addition, such a system can allow researchers to collect data without limitations of time and location. In this dissertation, a portable multi-sensor human motion analysis algorithm is been developed based on inertial measurement technology. The algorithm includes a newly designed coordinate flow chart analysis method to systematically construct rotation matrices for multi-Inertial Measurement Unit (IMU) application. Using this system, overhead throwing is investigated to reconstruct arm trajectory, arm rotation velocities, as well as torque and force imposed on the elbow and shoulder. Based on this information, different motion features can be established, such as kinematic chain timing as demonstrated in this work. Human subject experiments are used to validate the functionality of the method and the accuracy of the kinematics reconstruction results. Single axis rotation rig experiments are used to shown that this multi-IMU system and algorithm provides an improved in accuracy on arm rotation calculation over the conventional video camera based motion capture system. Finally, a digital filter with switchable cut-off frequency is developed and demonstrated in its application to the IMU-based sports motion signals. The switchable filter method is not limited only to IMUs, but may be applied to any type of motion sensing technology. With the techniques developed in this work, it will be possible in the near future to use portable and accurate sports motion analysis systems in training, rehabilitation and scientific research on sports biomechanics.

TABLE OF CONTENTS

LIST OF TABLES

LIST OF FIGURES

ACKNOWLEDGEMENTS

Although the dissertation I present here is my individual work, it could not be finished without the help from a lot of people. First of all, I would like to thank my advisor, Dr. William Clark, who brought me to this cutting edge research field and guided me to carry out research activities independently. His knowledge, experience and patience gave me confidence and helped me to conquer all difficulties in class study and research work. I also appreciate the valuable suggestions from the dissertation committee members: Dr. Daniel Cole, Dr. Nitin Sharma and Dr. Zhi-Hong Mao, which made my work stronger. The validation work is an essential part of this project. I had been carried out in Dr. Mark Redfern's lab, with the support from Dr. April Chambers, Jenna Montgomery and Grace Owens. I was so lucky to have a detailed tutorial on inertial measurement technology by Dr. Noel Perkins and Dr. Ryan McGinnis from University of Michigan. Their generous help let me gain a clear picture about my project. Besides, Dr. Richard Debski gave the first lesson on biomechanics and triggered the idea on throwing motion study. Dr. George Klinzing funded this project for one semester which helped me to keep the project during the most difficult time. Special thanks to Dr. John Metzger whom I served as teaching assistant for four semesters. The optimistic attitude on work and life I've learned from him will be my treasure in future. Of course, PhD was one of the biggest challenge not only on profession but also personal life. Without the support and love from my wife, parents and the whole family, as well as friends, I could not get to the end point.

1.0 INTRODUCTION

Ever since the beginning of the written history of human society, sports have been playing an important role in recreation, fitness, cultural communication and even politics. From the first organized Olympic Games in 776 BC to the soccer, baseball and golf leagues organized in many countries today, sports is no longer merely a way for entertaining but an enormous business that incents more and more people to become professional athletes. According to the statistics of the United States Department of Labor 16,500 jobs are registered as athletes and sports competitors. This number is predicted to increase by 22% until 2020, which is faster than the growth rate of other professions Besides professional athletes, ordinary people from everywhere of the world also enjoy the pleasure and healthy lifestyle from participation in sports activities, whether it involves well-equipped club games or street soccer popular in many developing countries. However, at the same time individuals gain the physical and mental benefits from sports, millions of people suffer injuries or asymptomatic pathologies, with different level of intensity, caused by drastic competition or inappropriate training. For example, a torn anterior cruciate ligament (ACL) will affect a soccer athlete's performance, and even suspend his or her career (Ekstrand, Hägglund et al. 2011), asymptomatic pathology of the shoulder or elbow joint is a common among baseball pitchers (Limpisvasti, ElAttrache et al. 2007), and 'tennis elbow' is a common injury for tennis players that requires long term treatment (Zeisig, Fahlström et al. 2010). Additionally, an increasing number of youth athletes experience serious injuries even

before starting a professional career (Emery, Hagel et al. 2010; Fleisig, Andrews et al. 2011). Two of the fast-growing trends in sports, commercialization and popularization, point to an increasing need for complete knowledge on sports biomechanics that can aid coaching, training, injury prevention and rehabilitation.

Towards this aim, both the academic community and professional sports teams have put enormous effort into studying the biomechanics underlying different types of sports motion. Within them, throwing motion has received intensive interest. As throwing is a rapid motion of the upper extremity that occurs in a short time, drastic stress and load is imposed on associated joints, thus increasing the injury risk level. However, more progress is necessary to fully understand the motion and its effects on joint health. Take the baseball pitching motion as an example, although numerous research works have been carried out in recent years to understand the relationship between pitching performance, associated joint load and injury risk, we still do not have conclusive knowledge regarding pitching biomechanics (Oyama 2012). Even in literatures, some conclusions disagree with each other. For example, researchers believe pitchers throwing higher velocity may be more susceptible to elbow and shoulder injuries (Bushnell, Anz et al. 2010; Hurd, Jazayeri et al. 2012). Werner et. al. (Werner, Suri et al. 2008), however, believes that higher ball velocity can be obtained by proper technique and does not necessarily incur high joint loads. One of the fundamental reasons for this slow progress is that the 'communication' between the academic society and sports participants, including professional teams, amateur players, and parents, is relatively low and inefficient. This judgment is explained in two ways: on one hand, coaches and athletes are hardly able to apply innovative research discoveries in training or real games because they cannot evaluate players' physical condition and performance in a quantitative and real-time way. For example, a recent study (Hurd, Jazayeri

et al. 2012) found elbow distraction force, or elbow adduction moment, is positively associated with pitching velocity, which suggested that talented high school pitchers may have higher possibility in elbow injury. Unfortunately, coaches cannot apply this knowledge in training to estimate injury risk for teen players, since there is no tool available to quantitatively monitoring the pitching motion, much less determine joint moment. On the other hand, the prevalent data collection methods for lab research involve the use of video cameras, and are carried out in restricted scenarios. Typically a target group of athletes is recruited to perform sports operations in a lab environment with a data collection setup that includes reflective markers attached to body segments. As is well known, performance is highly related to the level of cognitive and somatic anxiety, which is affected by environmental factors (Krane, Joyce et al. 1995; Craft, Magyar et al. 2003). As a result, it is reasonable to question that data and analysis results taken under a lab environment is more or less deviated from those under real training and game situations. Additionally, limited numbers of subjects and trials in lab research limits the generality of the conclusions (Oyama 2012). In order to overcome this dilemma and improve the communication efficiency between the academic society and sports industry, as well as potentially benefit non-professional sports amateurs on performance evaluation and injury prevention, this study focuses on the development of a low cost, portable sports motion analysis system based on inertial measurement technology. The system under study records body segment kinematics information, i.e. linear acceleration and rotation rate, to quantitatively reconstruct body segmental motion and to calculate kinetic quantities.

To validate the capability and demonstrate the applications of this inertial measurement based sports motion analysis system, this work has designed the system and data processing algorithm to be applicable to the throwing motion. It is able to quantitatively reconstruct the

body segmental trajectories and rotation velocities of the upper extremity motion, and calculate the joint moments and forces associated with the elbow and shoulder. It is worth mentioning that this system, including the motion reconstruction algorithm, can be used for any other type of sports motion with minor changes. Such a system will have promising applications in the following areas:

1) Training and coaching: real time accurate measurement of body motion will enable objective performance evaluation and instruction intervention;
2) Injury prevention: real time joint load monitoring and injury risk estimation;
3) Research: unlimited data collection and motion analysis under real training and game situations.

The framework of the motion analysis algorithm, which is designed to reconstruct both kinematics and kinetics of sports motion, is demonstrated in Figure 1. The 'IMU Deployment' block indicates that two IMUs were placed on the arm to study the throwing motion in this work. The coordinate flow chart is a newly designed graphical tool to visualize the coordinate frame transformation problem and systematically construct the rotation matrices. The kinematic reconstruction algorithm is designed to calculate body segment trajectories, linear/rotational velocity and so forth for kinematics analysis. The inverse dynamics model uses kinematics results, rotation matrices and anatomical parameters as inputs to calculate joint moments and force for kinetics analysis. The 'Low-pass filter' block indicates the digital filter designed in this work to process non-stationary sports motion signals.

Generally following the structure of the algorithm framework, this dissertation is organized as follows: Chapter 2 will provide background of the techniques used in this work and related literature; Chapter 3 introduces the coordinate flow chart method to analyze the coordinate frame

transformation problem and construct rotation matrices. This method will play an essential role in both of kinematics and kinetics analysis; Chapter 4 explains kinematics reconstruction as well as kinematic chain analysis of throwing; inverse dynamics model and kinetics analysis is explained in Chapter 5; towards the common non-stationary sports motion signal processing problem, a low pass filter with switchable cut-off frequency is introduced in Chapter 6; Chapter 7 presents conclusions for the work presented; a detailed sensor calibration procedure is described in the appendix.

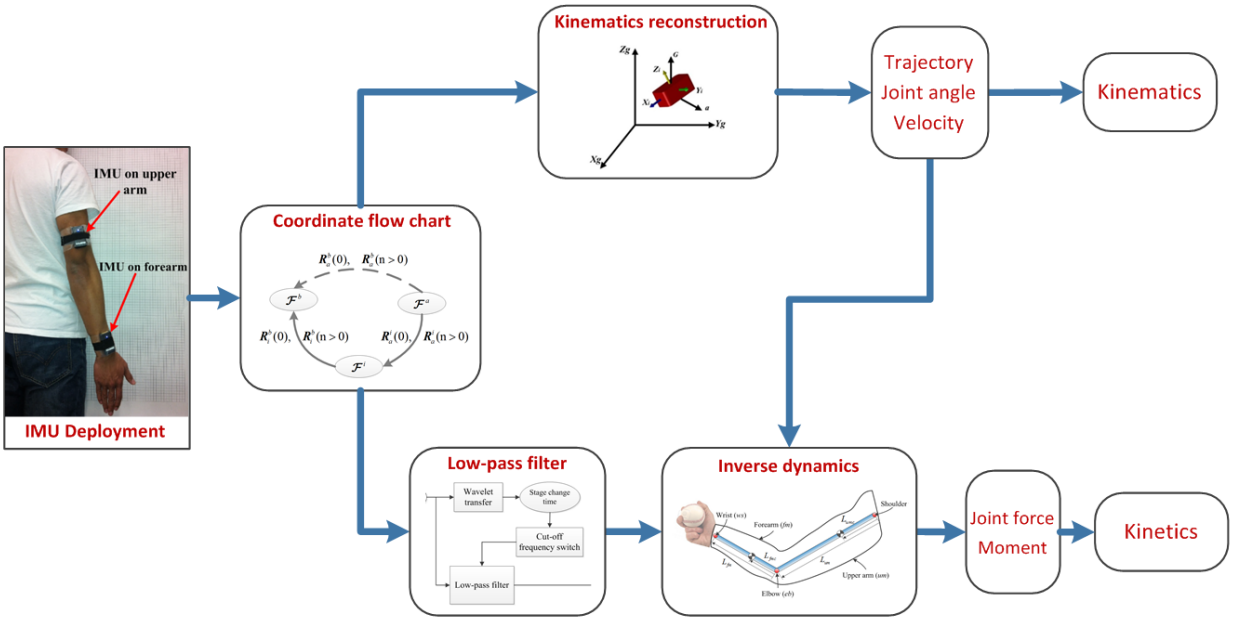

Figure 1 Framework of the motion analysis algorithm

2.0 BACKGROUND AND LITERATURE REVIEW

The throwing motion is the representative sports motion under investigation in this work. A multi-sensor alignment and motion analysis strategy will be designed to be adapted to throwing motion analysis. It is worth mentioning that work described in the following chapters can be readily adjusted and expanded to any kind of sports motion. This chapter briefly reviews the studies on throwing motion and current methods for motion capture, and then emphasizes the overview of inertial measurements for human motion study.

2.1 THE KINEMATIC CHAIN OF THROWING

A typical throwing motion can be pitching a baseball, spiking a volleyball, throwing a football and serving a tennis ball, etc. A key goal of the thrower is to generate the highest possible speed of the distal end of the upper extremity, i.e. hand. However, due to the limited capability of muscles associated with wrist and hand, an efficient pitching technique cannot merely rely on these muscles to generate desired throwing velocity. Pitchers usually make use of the sequencing movement of the whole body to accumulate moment from proximal to distal, e.g. movements of body segments are incited as the sequence of lower extremity, hip, upper torso, upper arm, forearm, and finally hand. This sequence is called the kinematic chain (Hirashima, Kadota et al. 2002; Hirashima, Yamane et al. 2008; Seroyer, Nho et al. 2010). Early researchers identified the

kinematic chain sequence timing by linear velocity of body segment ends. For example, the velocity magnitude of the hip, shoulder, elbow and wrist reach their peak values in sequence. Marshall et. al. (N. Marshall and Elliott 2000) revealed the important role of long-axis rotations of the arm segments in the kinematic chain during the tennis serve, which is also considered as an overhead throwing motion. Thus, this dissertation will use body segment rotational velocity to determine the kinematic chain timing.

Recent work found that a proper coordination of the kinematic chain will not only improve performance, but also reduce the risk level of injuries. Aguinaldo et. al. (Aguinaldo, Buttermore et al. 2003) found that higher level pitchers have delayed trunk rotation with less humeral internal rotation torque. Werner et al (Werner, Suri et al. 2008) have related some of the temporal and spatial characteristics of kinematic chain to the ball velocity, for instance a shorter interval between the events of stride foot contact and maximum shoulder external rotation is in favor of increased ball velocity. Although academic society has agreed that knowledge of optimizing throwing mechanics, i.e. the coordination of the kinematic chain, can provide valuable information for training, injury prevention, rehabilitation and performance improvement (Limpisvasti, ElAttrache et al. 2007), limited research has been done in detailed study of the kinematic chain of throwing. Seroyer, et. al. (Hirashima, Yamane et al. 2008) provided a spatial description of a proper kinematic chain of overhead pitching from a professional pitcher. However, this study involved qualitative visual assessment, and was carried out with a complex high speed camera setup. Sakiko Oyama (Oyama 2012) reviewed the state-of-the-art in biomechanics studies of the baseball pitching mechanism, and pointed out that a potential barrier to acquiring knowledge of 'proper' pitching technique is the unavailability of appropriate motion capture tools. Still in the same review paper, authors also noted that most injury related

research included limited number of subjects and trials, which limited the generalizability of these conclusions.

The inspection of literature mentioned above indicates that quantitative reconstruction of the kinematic chain can provide important information on performance evaluation, injury prevention and rehabilitation. For this reason, a tool that is able to capture the kinematic information and then reconstruct the spatial and temporal sequence of the kinematic chain will be preferred by coaches, physicians and sports biomechanics researchers.

2.2 OVERVIEW OF MOTION CAPTURE TECHNOLOGIES

Nowadays, the prevalent method to learn human motion biomechanics is using vision based motion capture systems. The commercial solutions are available from Motion Analysis Corporation (MotionAnalysis 2013), Vicon (Vicon 2013), Qualysis AB (Qualisys 2013), etc. As shown in Figure 2, the principle of this kind of system is to use cameras to capture light reflected by retro-reflective markers and determine the markers' locations in a pre-defined coordinate frame.

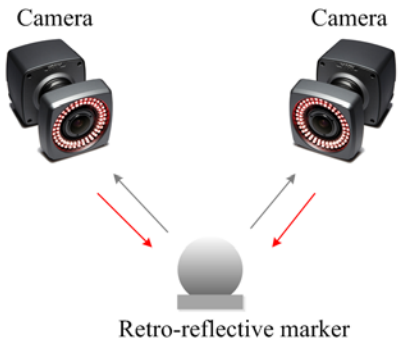

Figure 2 Demonstration of vision based motion capture system

The typical accuracy level when measuring low speed and small range of motion is 63±5 micron (Windolf, Götzen et al. 2008). Besides providing the kinematics, the time-location data can be input into inverse dynamics models, for instance, OpenSim (Delp, Anderson et al. 2007), to calculate segmental and joint forces and moments incurred by motion. Despite the popularity of the vision based technique in biomechanics studies, some inherent limitations of these systems have hindered the research progress, especially in high speed sports motion study. The video cameras are usually working at a speed of 200 fps. One may get 1000 fps capability with a costly hardware setup, such as Vicon T10S (Vicon 2013). Some peak events in sports motion change abruptly over a very short duration, for instance, the total time of a typical baseball pitching motion is 0.145 sec and the acceleration part (from maximum upper arm external rotation to ball release) is 0.029 sec (Stodden, Fleisig et al. 2005), which means a video camera can obtain 29 samples for the complete pitching event and only 6 samples for the acceleration stage if working at 200 fps. Besides, data collection volume is also limited due to file limitation, complex setup as well as other factors (Barris and Button 2008) .

Another essential limitation has been discussed more frequently in recent years. While using the marker location data to calculate the linear (and or angular) velocity (and/or acceleration), numerical derivatives are unavoidable in data processing, which implies measurement error and signal noise will be magnified. This situation can be even worse when high speed motion is involved, such as jumping, falling, and typical sports operations. In order to suppress noise introduced by numerical differentiation, a low-pass digital filter is usually applied to location data recorded by optical instruments. However, this low-pass filter will also distort those high speed motion signals of interests since they consist of components distributed in the high

frequency domain (Ismail and Asfour 1999; Wachowiak, Rash et al. 2000; Kristianslund, Krosshaug et al. 2012; Loh, Li et al. 2012).

In recent years, the markerless video camera based motion capture system has received more and more attentions. Based on computer vision technology, it is able to identify subjects' movements without deployment of markers. An example product based on this technology is Microsoft Xbox Kinect, as shown in Figure 3. Although it has improved mobility compared to the marker based video camera system, it still has most of the disadvantages of video camera systems. Besides, it has additional limitations on small segment motion detection, and background noise removal. (Weinland, Ronfard et al. 2011).

Figure 3 Microsoft Xbox Kinect

A second type of motion capture system makes use of bending sensors to measure joint angles, such as the CyberGlove demonstrated in Figure 4. It is designed for one degree freedom angle measurement. However, it suffers from the same numerical differentiation error issue as that of video camera system.

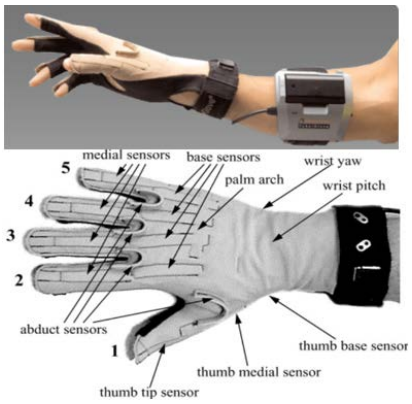

Figure 4 CyberGlove II (CyberGlove)

Another kind of motion capture device makes use of magnetism as an external signal source, for example the hand and finger motion capture device as shown in Figure 5 (Ma, Mao et al. 2011). The combination of magnetic signals received by the sensor array attached on the wrist are used to identify the position and attitude of fingers (Vinjamuri, Crammond et al. 2009; Ma, Mao et al. 2011). This idea can be a good choice when the motion of interest is in a limited range, in which case reference magnets and sensors can be deployed closely to avoid environmental interference. However, as for the motion to be reconstructed in this study which features high speed and large range of motion, it is difficult to deploy magnets and sensors to identify arm motion during throwing.

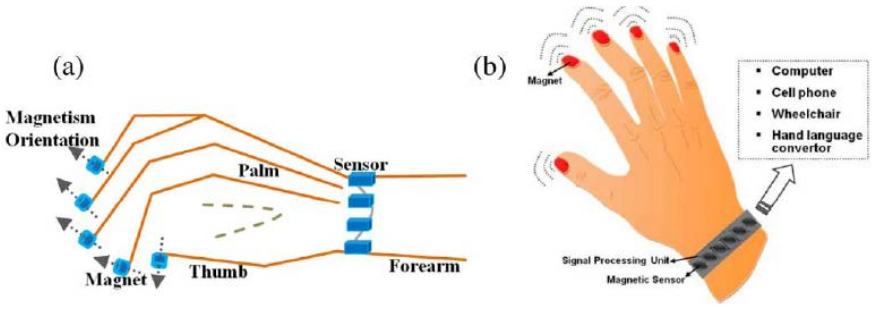

Figure 5 Structure of the magnetic hand motion tracking system (Ma, Mao et al. 2011)

Due to the requirement on high speed sports motion analysis and inherent limitations of current motion capture technologies, researchers and physicians are looking for alternatives. Among them, the inertial measurement technology is a promising candidate.

2.3 INERTIAL MEASUREMENT TECHNOLOGY

The term inertial measurement sensor in this study refers to a microelectromechanical (MEMS) gyroscope or accelerometer. The commercially available inertial measurement unit (IMU) integrates one or several gyroscopes and accelerometers with appropriate alignment to detect multi-axis angular rate and linear acceleration respectively. Some units may also include MEMS magnetometers. Although magnetometers do not measure motion using inertial transduction methods, their measurement of environmental magnetism can also be made useful in data processing algorithms designed in this work. With the fast developing MEMS manufacturing technology, MEMS inertial sensors are becoming smaller and more capable. The following sections offer a brief overview of inertial sensors and inertial measurement units on the market.

2.3.1 Angular Rate Gyroscopes

The MEMS gyroscope is based on Coriolis effect (Liu, Zhang et al. 2009) with a simplified structure shown in Figure 6 (Piyabongkarn, Rajamani et al. 2005). The vibrating mass reacts to the Coriolis acceleration while the inertial frame of the sensor undergoes a rotation. Nowadays, some commercially available gyroscopes, for example, ST L3G4200D (STMicroelectronics 2013) with the working scenarios shown in Figure 7, use a single driving mass to detect three

axes of rotation, which allow even smaller packaging and lower cost. The driving mass consists of four parts: M1, M2, M3 and M4. While rotation is applied along each axis, the corresponding part of the driving mass will be deflected, and thus generate different output.

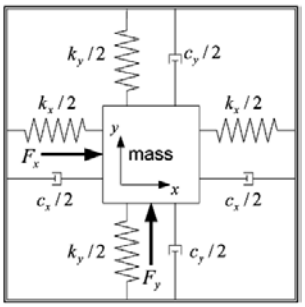

Figure 6 Simplified structure of suspended mass vibrating gyroscope (Piyabongkarn, Rajamani et al. 2005)

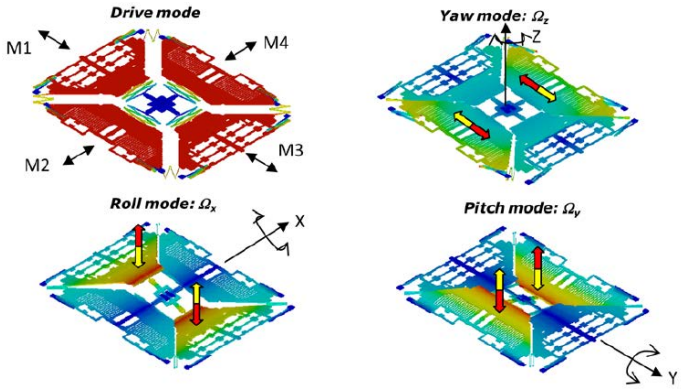

Figure 7 Demonstration of single driving mass gyroscope (STMicroelectronics 2013)

2.3.2 Accelerometers

In the inertial sensing market, MEMS accelerometers can be categorized according to the type of its sensing scheme: capacitive, piezoelectric, piezoresistive, resonance, etc. Within them, the capacitive type has many advantages compared to its counterparts: good DC response and noise performance, high sensitivity, relatively low drift and low temperature sensitivity (Acar and

Shkel 2003). For this reason, the capacitive MEMS accelerometer is popular in IMU design. A typical structure of the capacitive MEMS accelerometer consists of suspended silicon structures attached to the substrate that is free to move depending on the sensed acceleration. Differential capacitors are constructed by independent fixed plates and plates attached to the moving mass. The simplified transducer model is shown in Figure 8 (Freescale 2008). When the sensor undergoes acceleration, the proof mass deflects from its nominal position, causing an imbalance in capacitance between the fixed plates and moving plates. This imbalance will be measured and interpreted as acceleration.

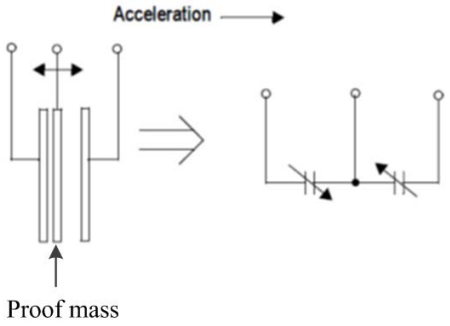

Figure 8 Simplified transducer physical model (Freescale 2008)

Nowadays, some manufacturers have integrated 3-DOF accelerometer, 3-DOF gyroscope and 3-DOF magnetometer into a single chip with only 4×4×1(mm) size , for instance, MPU-9150 from InvenSense Inc. (InvenSense 2013). Manufacturers have made available sensor chips that contain orthogonal combinations of rate gyros, accelerometers, and magnetometers. Selected commercial sensor chips are listed in Table 1.

2.3.3 Magnetometers

Magnetometer is not a type of inertial sensor. However, MEMS magnetometers are often applied together with other inertial sensors to provide the heading angle by comparing the magnetic field

direction reading of magnetometer and the pre-calibrated local environment magnetic field. Magnetometers can be classified into three categories depending on their measurement range of the magnetic field strength: low filed (<1 micro Guass), medium field which is also termed as earth's field (1mG – 10G) and high field or bias magnet field(>10G) (Caruso, Bratland et al. 1998).

Table 1 Selected commercial inertial sensor chips

Manufacturer	Model	Category	Gyroscope (°/s)	Accelerometer (g)	Compass	Output	Size (mm)
InvenSense	MPU-9250	acc, gyro, compass	±2000	±16	±4900μT	I^2C	3×3×1
	MPU-6050 MPU-6100	6DOF acc & gyro	±2000	±16	NA	I^2C	4×4×0.9
	MPU-3050	3DOF gyro	±2000	NA	NA	I^2C	4×4×0.9
	ITG-3200	3DOF gyro	±2000	NA	NA	I^2C	4×4×0.9
ST	LIS331HH	3DOF acc	NA	±24g	NA	I^2C /SPI	3×3×1
	L3G4200D	3DOF gyro	±2000	NA	NA	I^2C /SPI	3×3×1.1
Honeywell	HMC5883L	3DOF compass	NA	NA	±8 Gauss	I^2C	3×3×0.9
AsahiKASEI	AK8975	3DOF compass	NA	NA	±1200μT	I^2C	4×4×0.75

The common technologies for designing of magnetometers include: search coil, fluxgate, SQUID, anisotropic magnetoresistance (AMR), giant magnetoresistance (GMR) and etc. The measurement range of different technologies are demonstrated in Figure 9. Thus, depending on the requirements of practical applications, one should choose magnetometers which are designed by appropriate technology. In human motion tracking applications, magnetometers measure the relative direction change of earth's magnetic field with respective to the sensor's frame. The AMR sensors are ideal candidate for this type of applications.

The AMR sensor is made of a nickel-iron (or Permalloy) thin film deposited on a silicon wafer and is patterned as a resistive strip. Changes of both of magnitude and direction can be represented by the voltage output of the Wheatstone bridge of four resistive strips as shown in

Figure 10. An example product designed by the AMR technology is Honeywell HMC5883L which has a measurement range from milli-Gauss to 8 Gauss (Honeywell).

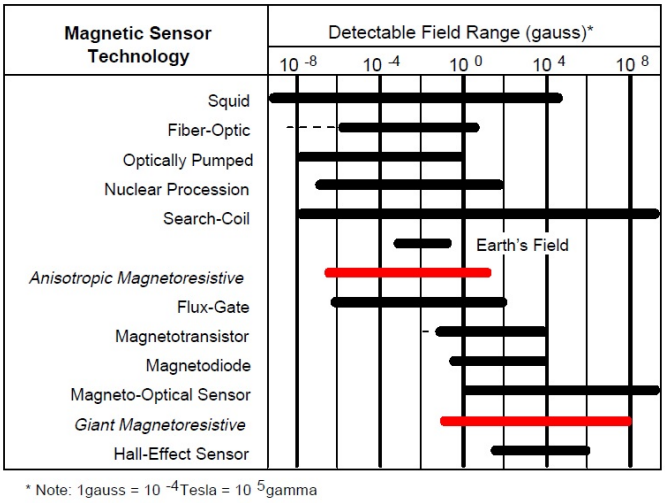

Figure 9 Measurement range of magnetometers (Caruso, Bratland et al. 1998)

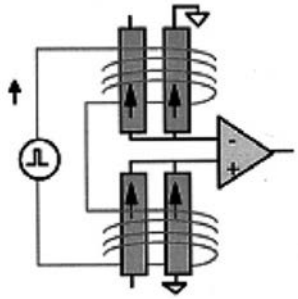

Figure 10 Circuit demonstration of the AMR sensor (Lenz and Edelstein 2006)

2.3.4 Inertial Measurement Units

The inertial measurement unit is a combination of inertial sensor chips, data transmitting or storage elements and other peripheral circuits. Depending on the application requirement, different types of sensors with different numbers of degrees of freedom (DOF) can be combined

to construct the sensing element of an IMU. For example, one gyroscope with one sensitive axis and an accelerometer with two sensitive axes can be used to construct a 3 DOF IMU to measure 2 dimensional plane motion. On the market, there are some vendors that provide IMUs which are ready to use, such as Xsens (Xsens 2013), YEI corporation (Yost Engineering 2013), and Microstrain (MicroStrain 2013). These IMUs have different capability of sensitivity axes, sensing range, and data transmitting and storage method. The specifications of selected IMU products are listed in Table 2.

Table 2 Selected commercial IMU with specifications

Vendor	Model	Accelerometer		Gyroscope		Magnetometer	
		DOF	Range	DOF	Range (°/s)	DOF	Rnage
Xsens	MTx	3	± 50 (m/s^2)	3	± 1200	3	± 750 (mGa)
	MTi 100	3	± 50 (m/s2)	3	± 450	3	± 2 (Ga)
YEI	3-Space Data-logging (high-G)	3	±6 / ±12 / ±24 (g)	3	±250 / ± 500 / ± 2000	3	± 1.3 (Ga)
	3-Space Wireless 2.4GHz	3	±2 / ±4 / ±8 (g)	3	±250 / ± 500 / ± 2000	3	± 1.3 (Ga)
MicroStrain	3DM-GX3-15	3	±5 (g)	3	± 300	NA	

Based on the motion range and preferred data transmitting/storage method, one can pick a commercially available IMU for a specific application. The current study, which features high speed sports motion, requires high range accelerometers and gyroscopes to capture the motion data without saturation. The YEI 3-Space Data-logging (high-G) provides the highest available accelerometer and gyroscope range at the same time, which is ±24 (g) and ± 2000 (°/s) respectively. However, strictly speaking, this range is still not enough for a throwing motion study. In the baseball pitching motion, the reported upper arm internal rotation of a skilled adult is up to 7,000 (°/s) (Fleisig, Andrews et al. 1995). Since the goal of this work is to establish a motion analysis system with data processing algorithm, ± 2,000 (°/s) angular velocity range is

enough to validate the functionality and demonstrate applications. In order to avoid the gyroscope output saturation, subjects will carry out the throwing motion in a low level of exertion. In the case of performance evaluation during real games and training, higher range of gyroscope must be integrated to sense the body segment rotation along its longitudinal axis. Recently, Analog Device has released a single axis high range gyroscope, ADXRS649, which is able to measure up to 20,000 (°/s) angular velocity (Devices 2011). This high range gyroscope sensor has not been integrated into any commercially available IMU product. The motion analysis algorithm presented in this thesis can be easily adjusted to incorporate the higher measurement unit as soon as they are available to customers.

2.4 BIOMECHANICS APPLICATIONS OF INERTIAL MEASUREMENT UNIT

In 2002, Mayagoitia et. al. (Mayagoitia, Nene et al. 2002) proposed a motion capture system solely based on MEMS accelerometers and gyroscopes as an alternative method to the optical motion capture system. This inertial sensor based system was limited to reconstructing 2-dimensional kinematics. Also, the method required perfect alignment of the sensors to the body coordinates. Since then, inertial measurement has become a promising technique for human motion capture and analysis, and has been the focus of many studies.

According to the characteristics of the specific motion under study, these works are categorized into slow motion and fast motion. In this study, slow motion includes daily human motions which are usually in a relaxing and comfortable tempo, for instance, walking, drinking, writing and etc. The fast motion is defined to include much more intense motions, such as jumping, throwing and kicking. Most sports motions fall into the category of fast motion. Based

on the content to be reconstructed, they can be categorized into kinematics study and inverse dynamics study. The difference is that kinematics studies involve the calculation of velocity, acceleration, and body segment position and attitude, whereas inverse dynamics studies use the kinematics information as well as the human body parameters to analyze the joint moments, forces or torques applied on body segments. As a result, the two criteria will divide these works into four categories shown in Figure 11: 1) kinematics study on slow motion; 2) kinematics study on fast motion; 3) kinetics study on slow motion and 4) kinetics study on fast motion.

It is obvious in Figure 11 that most inertial measurement work has focused on studying kinematics of slow motion, including gaiting analysis (Mayagoitia, Nene et al. 2002; Sabatini 2005), reconstructing lower extremity joint angle such as knee, ankle and feet during slow daily movement (O'Donovan, Kamnik et al. 2007; Favre, Jolles et al. 2008; Cooper, Sheret et al. 2009; Favre, Aissaoui et al. 2009; Liu, Liu et al. 2009; Rouhani, Favre et al. 2011; Rouhani, Favre et al. 2012), and upper extremity attitude and joint angle reconstruction (Sabatini 2006; Luinge, Veltink et al. 2007; Cutti, Giovanardi et al. 2008; De Vries, Veeger et al. 2010; Schepers, Roetenberg et al. 2010; El-Gohary and McNames 2012; Lee and Low 2012). Different methods have been investigated, which can be generally summarized into two categories: strap-down integration (Sabatini 2005) and optimal filters (Sabatini 2006). In the kinematics study of fast motion, investigators have used inertial sensors to study sports motions, such as baseball pitching (Sagawa, Abo et al. 2009; Koda, Sagawa et al. 2010), baseball bat swing (Ghasemzadeh and Jafari 2011) and skiing (Chardonnens, Favre et al. 2012). In this area, researchers are interested in not only reconstructing kinematics quantities, but also interpreting these quantities into sports performance indicators, for instance reconstructing kinematic chain timing (Ghasemzadeh and Jafari 2011; Chardonnens, Favre et al. 2012).

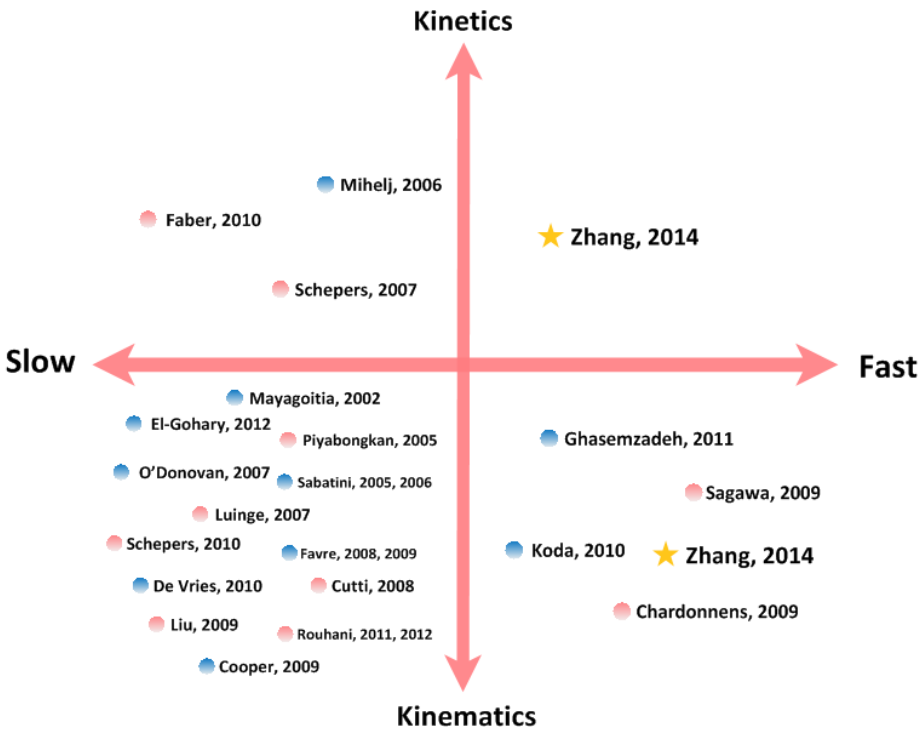

Figure 11 Categories of inertial measurement studies based motion analysis work

Since the inverse dynamics problem is more complicated, only a few works have been related to kinetics study of slow motion (Mihelj 2006; Schepers, Koopman et al. 2007; Faber, Kingma et al. 2010). No studies could be found on the topic of studying kinetics of fast motion using inertial sensors. One of the reasons for this unbalanced distribution is that the inertial sensor capability has been limited as explained in the previous section. With the increasing measurement range of accelerometers and gyroscopes, academic society will pay more attention to using inertial sensors to analyze fast motion, especially sports motions. The multi-sensor based sports motion analysis strategy presented in this thesis will begin to fill the gaps in using inertial sensor for fast motion analysis, both kinematics and kinetics, as shown in Figure 11.

3.0 COORDINATE FRAME TRANFORMATION AND ROTATION MATRIX CONSTRUCTION

The commercially available IMU used in this study is 3-Space Data-logging sensor (YEI Technology TSS-DL-HH) illustrated in Figure 12. It integrates three types of sensors: a tri-axial accelerometer, a tri-axial rate gyroscope and a tri-axial magnetometer. The accelerometer and gyroscope record linear acceleration and angular velocity, respectively, of the IMU itself in a synchronous way, while the magnetometer detects magnetic field of the environment. However, in biomechanics applications, the task of IMUs is reconstructing not only its own motion, but also the dynamics of body segments on which these sensors are attached. Assuming the arm segments are rigid bodies, two IMUs are able to provide sufficient information for arm motion analysis. As shown in Figure 13, one IMU is attached on the wrist, while the other one is attached on upper arm. The algorithm established in the following sections does not have strict requirements on the IMU's location.

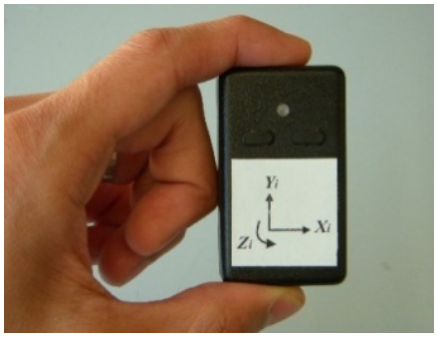

Figure 12 The IMU with sensitive axes label

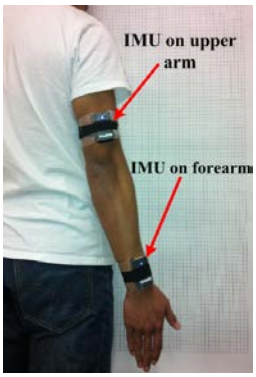

Figure 13 IMUs on the pitching arm

3.1 INTRODUCTION OF COORDINATES FLOW CHART

In order to obtain anatomical motion quantities, for example, shoulder internal/external rotation, kinematic quantities captured by IMUs should be transformed to corresponding anatomical coordinate frames. The deployment in Figure 13 indicates that a total of five coordinate frames need to be defined, which are shown in Figure 14. The name of each coordinate frame and its axes is listed as follows:

$\boldsymbol{F}^{g}$ (X_{g}, Y_{g}, Z_{g}): global coordinate frame;

$\boldsymbol{F}^{um}$ (X_{um}, Y_{um}, Z_{um}): upper arm coordinate frame;

$\boldsymbol{F}^{ium}$ (X_{ium}, Y_{ium}, Z_{ium}): coordinate frame of IMU deployed on upper arm;

$\boldsymbol{F}^{fm}$ (X_{fm}, Y_{fm}, Z_{fm}): forearm coordinate frame;

$\boldsymbol{F}^{ifm}$ (X_{ifm}, Y_{ifm}, Z_{ifm}): coordinate frame of IMU deployed on forearm.

The axis directions of the five coordinate frames are determined as follows: the direction of global frame $\boldsymbol{F}^{g}$ is defined according to the specific project. In this study, Y_g is horizontal and

toward the throwing target, while X_g is perpendicular to Y_g and points to the right side if the subject is standing face to the target. The axis directions of the two IMUs are pre-defined and labeled as shown in Figure 12. The two anatomical frames, $\boldsymbol{F}^{um}$ and $\boldsymbol{F}^{fm}$ are defined while the throwing arm is in anatomical neutral posture: subject is standing still with arm pointing vertically downward, elbow fully extended and palm facing towards anterior direction (as shown in Figure 13). Then the origins of the two frames are fixed to the distal ends of the two arm segments respectively, i.e. elbow and wrist. The longitudinal axes of the two arm segments, forearm and upper arm, are defined as Z_{fm} and Z_{um} respectively, with their senses being positive in the vertically upward direction. Y_{fm} and Y_{um} are horizontal and towards the anterior direction, while X_{fm} and X_{um} are also horizontal and towards lateral direction. The anatomical frames are fixed to their respective body segment as soon as they are defined. A special case that is useful in calibration and in setting up the initial attitude is when the subject stands on the test field, faces the target with throwing arm in anatomical neutral posture, the coordinate frames $\boldsymbol{F}^{um}$, $\boldsymbol{F}^{fm}$ and $\boldsymbol{F}^{g}$ are aligned with each other, but with their origins offset by fixed translations.

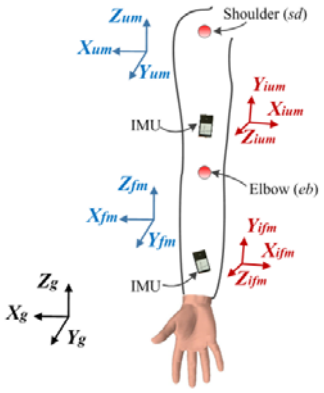

Figure 14 Definition of coordinate frames

In three dimensional human motion analysis, anatomical, kinematic and kinetic quantities are represented by 3×1 vectors which are written as $\vec{v}_1^2$ in this work. The subscript 1 represents

content of this vector while the superscript 2 indicates the coordinate frame in which this vector is expressed. For example, the relative position of shoulder to elbow is a vector which can be represented in upper arm frame as $L_{sd/eb}^{um} = [0 \quad 0 \quad l]^T$, where l is the length of the upper arm. When the attitude of the upper arm needs to be determined, this vector must be expressed in the global coordinate frame, i.e. $L_{sd/eb}^{g}$ to provide meaningful information. In this example, $L_{sd/eb}^{um}$ and $L_{sd/eb}^{g}$ are the same vector in space, but expressed in two different coordinate frames: $\boldsymbol{F}^{um}$ and $\boldsymbol{F}^{g}$ respectively. This coordinate frame transformation of a vector expression can be realized by a rotation matrix. A rotation matrix is a 3×3 matrix in 3 dimensional space, and is written as R_a^b in this work. R_a^b represents transformation of a vector expression from frame a to frame b. According to the matrix theory, a pure rotation matrix without scaling has the following properties:

Property 1: $$\vec{v}_1^b = R_a^b \cdot \vec{v}_1^a \quad (1)$$

Property 2: $$R_a^b = (R_b^a)^T \quad (2)$$

Property 3: $$\|r_i\| = \|c_j\| = 1 \ (i = 1,2,3 \quad j = 1,2,3) \quad (3)$$

Property 4: $$r_i \cdot r_j = 0 \ and \ c_i \cdot c_j = 0 \ (i = 1,2,3 \quad j = 1,2,3 \quad i \neq j) \quad (4)$$

Property 5: $$R_a^b = R_{n-1}^b \cdot R_{n-2}^{n-1} \cdots R_1^2 \cdot R_a^1 \quad (5)$$

where r_i means row i and c_j means column j of any rotation matrix R_a^b . In *Property* 1, $\vec{v}_1^a$ and $\vec{v}_1^b$ are the same vector but represented in $\boldsymbol{F}^a$ and $\boldsymbol{F}^b$ respectively. The rotation matrix R_a^b transforms the vector expression from $\boldsymbol{F}^a$ to $\boldsymbol{F}^b$ without changing the physical quantity of the vector. *Property* 2 indicates the opposite direction of coordinate frame transformation can be realized by transpose of the rotation matrix. *Property* 3 means the magnitude of each row r_i and column c_j is unity; this property is valid for pure rotation without scaling. *Property* 4 indicates orthogonality

between rows or columns. *Property* 5 indicates that the combined effect of multiple coordinate frame transformations is equal to a single transform from the start frame to the end frame.

The coordinate frame transform analysis could be simple and intuitive when a small number of frames are involved. However, as more and more IMUs are networked to study the arm segments and even the whole body motion, a large number of coordinate frames are involved which imply a complicated and sometimes tedious analysis and calculation. Inspired by the finite-state machine (FSM) theory in computer programming (Chow 1978) and discrete event system control (Ramadge and Wonham 1989), a graphical tool is designed to deal with the coordinate frames transform issue, which is named the Coordinate Flow Chart (CFC) in this work.

Elementary components constructing a CFC include *coordinate frame*, *transform line*, and *transform condition*. Figure 12 depicts a sample CFC. A coordinate frame is represented by an ellipse, which is labeled by its name. Transform lines (solid or dashed) connect any two frames with an arrowhead indicating the transform operation direction. The transform condition is associated with a transform line, and consists of a time series of rotation matrices that transform the vector expression from current frame to target frame at every time instant. Since in real applications, the initial rotation matrix and its following instantaneous rotation matrices are usually obtained by different mathematical methods, the transform condition is explicitly written as initial transform condition $R_a^b(0)$, and instantaneous transform condition $R_a^b(n > 0)$ (that is, a rotation at any time instant after the initial time).

Two basic coordinate frame transform scenarios are defined as direct transform (Figure 15), and indirect transform (Figure 16). A transform operation is considered to be direct when the transform conditions, both initial rotation matrix $R_a^b(0)$ and instantaneous rotation matrices

$R_a^b(n>0)$, can be obtained by methods established in section 3.3 (IMU-body segment alignment procedure) and 3.4 (instantaneous rotation matrix updating procedure) . For example, the transform between the IMU frame and the body segment it is attached on can be obtained by the alignment procedure explained in section 3.3. However, the transform between the IMU frame and the body segment frame the IMU is not attached on, for instance transform between an IMU attached on the forearm and the upper arm anatomical frame, has to involve other coordinate frame transform operations. This will be considered as an indirect transform.

In a direct frame transform scenario, shown as Figure 15, the line on the top demonstrates a transform operation from $\boldsymbol{F}^a$ to $\boldsymbol{F}^b$ which is realized by rotation matrices $R_a^b(0)$ and $R_a^b(n>0)$. The line on the bottom has an opposite direction indicating transform operation from $\boldsymbol{F}^b$ to $\boldsymbol{F}^a$. From *Property* 2 of rotation matrices, it is obvious that when a transform condition of one transform direction is obtained, the opposite direction can be easily calculated by the matrix transpose operation.

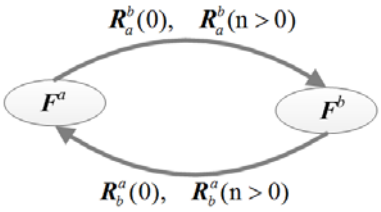

Figure 15 Direct frame transform

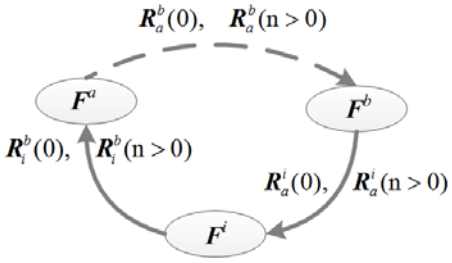

Figure 16 Indirect frame transform

When the rotation matrices between two coordinate frames are not available, an indirect frame transform can be established via intermediate frame(s). For instance, in Figure 16, the frame transform operation from $\boldsymbol{F}^a$ to $\boldsymbol{F}^b$ is achieved by two intermediate steps of transform:

$$\boldsymbol{F}^a \rightarrow \boldsymbol{F}^i: R_a^i(0), R_a^i(n>0) \quad (6)$$

$$\boldsymbol{F}^i \rightarrow \boldsymbol{F}^b: R_i^b(0), R_i^b(n>0) \quad (7)$$

From *Property* 5, the indirect frame transform steps can be combined as:

$$\boldsymbol{F}^a \rightarrow \boldsymbol{F}^b: \begin{cases} R_a^b(0) = R_i^b(0) \cdot R_a^i(0) \\ R_a^b(n>0) = R_i^b(n>0) \cdot R_a^i(n>0) \end{cases} \quad (8)$$

The number of intermediate frames can be more than 1 in large scale coordinate frame network. While multiple intermediate frames are involved, the transform condition is obtained by multiplication of transform matrices following the sequence of the transform path.

3.2 COORDINATE FLOW CHART OF THROWING ARM

As shown in Figure 14, five coordinate frames have been defined for motion analysis of two arm segments during throwing. Based on the coordinate flow chart theory introduced in the previous section, the CFC of a two-segment throwing arm is constructed in Figure 17: two IMU frames $\boldsymbol{F}^{ium}$ and $\boldsymbol{F}^{ifm}$, two anatomical frames $\boldsymbol{F}^{um}$ and $\boldsymbol{F}^{fm}$, and the global frame $\boldsymbol{F}^g$ are placed at arbitrary topology. Four direct transforms can be built and demonstrated by solid lines:

$\boldsymbol{F}^{ium} \rightarrow \boldsymbol{F}^g$: transform from upper arm IMU frame to global frame;

$\boldsymbol{F}^{ifm} \rightarrow \boldsymbol{F}^g$: transform from forearm IMU frame to global frame;

$\boldsymbol{F}^{ium} \rightarrow \boldsymbol{F}^{um}$: transform from upper arm IMU frame to upper arm frame;

$\boldsymbol{F}^{ifm} \rightarrow \boldsymbol{F}^{fm}$: transform from forearm IMU frame to forearm frame;

These direct transform conditions can be obtained by IMU and arm segment alignment procedure (section 3.3), IMU initial attitude calibration procedure (section 3.4.1), and instantaneous IMU attitude updating procedure (section 3.4.2). To simplify the CFC, the transform line is only shown in one direction. Three indirect transforms are indicated by dashed lines in Figure 17 which can be obtained by combined direct transforms.

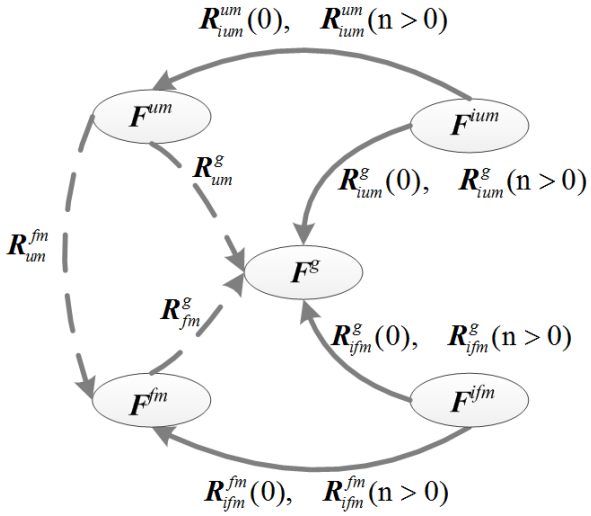

Figure 17 CFC of two segment pitching arm

3.3 ALIGNMENT MATRIX

The alignment matrix is the rotation matrix that correlates the IMU coordinate frame and that of the corresponding body segment to which the IMU is attached. In this work, two alignment matrices need to be established, R_{ium}^{um} and R_{ifm}^{fm}. In some applications, the IMU is considered to be attached firmly with its coordinate axes coinciding with the subject's axes (Liu, Liu et al. 2009; Sagawa, Abo et al. 2009; El-Gohary and McNames 2012). However, in real situations,

especially human motion analysis, the alignment cannot be guaranteed due to the uneven muscle surface. Thus, the misalignment between IMU frame and body segment frame is unknown and will dramatically degrade the accuracy of kinematics and dynamics reconstruction thereafter. In the work reported by Brennan et. al. (Brennan, Zhang et al. 2011), error caused by ignoring alignment matrix is evaluated using an instrument gimbal. The results demonstrated that the alignment is an important factor in evaluation of biomechanics using IMUs.

In the literature, various alignment methods have been proposed. They share a common idea: when a known direction motion, linear acceleration or rotation, is imposed on the IMU, the mathematical correlation that exists between the known motion vector and IMU digital reading vector is:

$$\vec{v}^b = R_i^b \cdot \vec{v}^i \qquad \textbf{(9)}$$

where $\vec{v}^b$ is the motion vector with known direction, linear acceleration or rotation along anatomical axes, while $\vec{v}^i$ is the sensor output vector recorded by IMU and represented in the IMU frame. Assume the body segment frame has axes ($X_b \quad Y_b \quad Z_b$) and the IMU frame has axes ($x_i \quad y_i \quad z_i$). The elements of the rotation matrix R_b^i can be written as (Diebel 2006):

$$R_b^i = \begin{bmatrix} \cos(X_b, x_i) & \cos(Y_b, x_i) & \cos(Z_b, x_i) \\ \cos(X_b, y_i) & \cos(Y_b, y_i) & \cos(Z_b, y_i) \\ \cos(X_b, z_i) & \cos(Y_b, z_i) & \cos(Z_b, z_i) \end{bmatrix} = \begin{bmatrix} X_x & Y_x & Z_x \\ X_y & Y_y & Z_y \\ X_z & Y_z & Z_z \end{bmatrix} \qquad \textbf{(10)}$$

where $\cos(X_b, x_i)$ means cosine of the angle between the two coordinate axes, X_b and x_i. When a motion vector along the X_b axis is imposed on the IMU, the normalized sensors triplet output is the first column of R_b^i. Repeating the same procedure for Y_b and Z_b will fully determine the 9 elements of R_b^i. The key is choosing appropriate motion vectors. Favre et. al.(Favre, Jolles et al. 2008; Favre, Aissaoui et al. 2009) applied hip abduction/adduction movement without any movement of knee joint, thereby allowing the alignment matrices of the IMUs on thigh and

shank to be determined. Luinge, H. et. al. (Luinge, Veltink et al. 2007) applies pronation and supination movement to align the IMU and forearm coordinate frames. In order to eliminate the effect of sensor noise, integration of gyroscope or accelerometer readings over time is usually used.

In this work, the alignment procedure is carried out after the IMUs have been firmly attached to the throwing arm of the subject. While the arm is in the anatomical neutral posture, the upper arm frame and forearm frame axes directions are defined as in Figure 18(a). The two anatomical planes, sagittal plane and coronal plane, are marked as *SP* and *CP* respectively as shown in Figure 18(b). The subject then performs the following two-step procedure:

Step 1: The subject stands still at the standard anatomical neutral posture for around 5 seconds to allow the accelerometers to record the vertical gravity vector which is coincident with anatomical axes Z_{um} and Z_{fm};

Step 2: The subject performs shoulder flexion/extension rotation in sagittal plane (*SP*) which lets the gyroscopes capture the angular velocity about the horizontal axis toward the lateral side, i.e. X_{um} and X_{fm}, shown as in Figure 18(b). The rotation is completed 5 times.

Mathematically, the process amounts to finding three unknown columns, $\boldsymbol{c}_i$, of the two alignment matrices, R_{ium}^{um} and R_{ifm}^{fm}, whose matrix form can be noted as $R_{i*m}^{*m} = [\boldsymbol{c}_1 \quad \boldsymbol{c}_2 \quad \boldsymbol{c}_3]$. The accelerometer readings from each IMU at *step 1* are marked as *STA* as shown in Figure 19. Acceleration reading over this quiet time is averaged and normalized to unity to get the third column $\boldsymbol{c}_3$ of the respective IMU's alignment matrix. One of the rotation direction (positive or negative) of gyroscope readings from each IMU at *step 2* are labelled as ROT_i, and integrated with respect to time and normalized to unity to get the vector $\boldsymbol{c}_1^t$. Then the second and first columns of the respective IMU's alignment matrices are calculated by Eqs. (11) and (12):

$$\boldsymbol{c}_2 = \frac{\boldsymbol{c}_3 \times \boldsymbol{c}_1^t}{\|\boldsymbol{c}_3 \times \boldsymbol{c}_1^t\|} \quad (11)$$

$$\boldsymbol{c}_1 = \frac{\boldsymbol{c}_2 \times \boldsymbol{c}_3}{\|\boldsymbol{c}_2 \times \boldsymbol{c}_3\|} \quad (12)$$

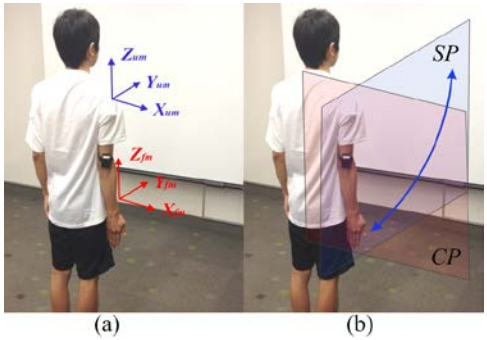

Figure 18 Alignment procedures; *SP*: sagittal plane, *CP*: coronal plane

Assuming the IMUs are firmly attached on the arm segments without relative motion, the instantaneous rotations are also determined by the alignment matrix, i.e.

$$\begin{cases} R_{ium}^{um}(0) = R_{ium}^{um}(n > 0) \\ R_{ifm}^{fm}(0) = R_{ifm}^{fm}(n > 0) \end{cases} \quad (13)$$

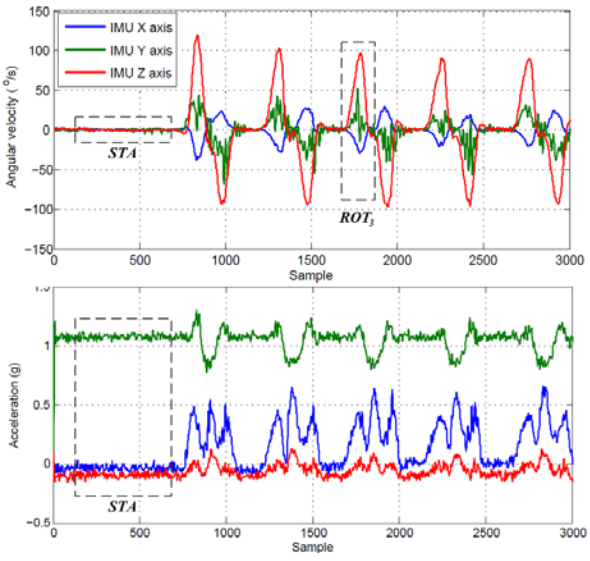

Figure 19 Alignment procedure data

3.4 QUATERNION BASED ROTATION MATRIX CONSTRUCTION

This section discusses another method to construct direct coordinate transforms between two frames in Figure 17, namely the transforms from the IMU frames to the global frame: $\boldsymbol{F}^{ium} \rightarrow \boldsymbol{F}^{g}$ and $\boldsymbol{F}^{ifm} \rightarrow \boldsymbol{F}^{g}$. While the IMU is moving arbitrarily in three dimensional space, the attitude of the coordinates X_i-Y_i-Z_i is changing all the time, indicated in Figure 20. Here subscript i stands for IMU frame, and could be either $\boldsymbol{F}^{ium}$ or $\boldsymbol{F}^{ifm}$. Meanwhile, the accelerometer is detecting the superposition of the vertically upward reactive force $\boldsymbol{GR}$ caused by gravity (Lobo and Dias 2003) and the IMU's linear acceleration $\boldsymbol{a}$. In other words, this combined acceleration is projected onto the IMU coordinate frame which has unknown attitude. In order to obtain the expression of IMU's linear acceleration $\boldsymbol{a}$ in global frame, the rotation matrices that relate the IMUs' frames to the global frame must be obtained to transform the acceleration expression in IMU frame to the global frame. In this two segment arm case shown in Figure 17, R^{g}_{ium} and R^{g}_{ifm} need to be determined.

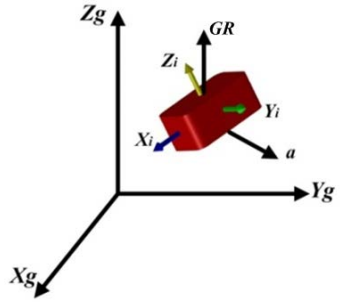

Figure 20 Acceleration measurement and coordinate frames

Several mathematical methods have been developed to describe the attitude of a rigid body and deal with the vector rotation problem, such as Euler angles, unit quaternion, direction cosine matrix and so forth (Diebel 2006). In this study, the quaternion based rotation matrix

construction technique is applied considering its ease of programming and calculation, as well as the fact that it does not have a singularity problem which is associated with the Euler angle representation (Diebel 2006). The Eq. (14) shows different forms of the four element quaternion. It has scalar part q_0 and vector part $\boldsymbol{e}$, which contains the rotation information that relates two different coordinate frames: frame 1 has rotated with respect to the unit direction vector $[u_x \quad u_y \quad u_z]$ through an angle θ to frame 2. According to the definition, the norm of the quaternion, calculated as in Eq. (15), must be unity in order to assure a pure rotation without scaling (Kuipers 1999; Diebel 2006).

$$\mathbf{q} = \begin{bmatrix} \boldsymbol{q_0} \\ \boldsymbol{q_1} \\ \boldsymbol{q_2} \\ \boldsymbol{q_3} \end{bmatrix} = \begin{bmatrix} \boldsymbol{cos\frac{\theta}{2}} & \boldsymbol{u_x sin\frac{\theta}{2}} & \boldsymbol{u_y sin\frac{\theta}{2}} & \boldsymbol{u_z sin\frac{\theta}{2}} \end{bmatrix} = \begin{bmatrix} \boldsymbol{q_0} \\ \boldsymbol{e} \end{bmatrix} \qquad (14)$$

$$\|\mathbf{q}\| = \sqrt{\boldsymbol{q_0^2 + q_1^2 + q_2^2 + q_3^2}} \qquad (15)$$

3.4.1 Initial rotation matrix

The initial quaternion represents the attitude of the IMU at the beginning of motion. While the IMU is in any stationary attitude, the only inertial force imposed on the accelerometer is the gravitational reactive force $\boldsymbol{GR}$, whose direction is strictly aligned with $+Z_g$ axis in the global coordinate frame. Consider the IMU on upper arm, i.e. *ium* for example, the normalization of the accelerometer output $\begin{bmatrix} a_x^{ium} & a_y^{ium} & a_z^{ium} \end{bmatrix}$ during this stationary period, which is shown as the right side of the Eq. (16), is the projection of the unit axis $+Z_g$ onto the $\boldsymbol{F}^{ium}$ coordinates:

$$[r_1 \quad r_2 \quad r_3] = \frac{\begin{bmatrix} a_x^{ium} & a_y^{ium} & a_z^{ium} \end{bmatrix}}{|\boldsymbol{GR}|} \qquad \textbf{(16)}$$

To reach the initial quaternion, the intermediate step is to calculate the corresponding Euler angles sequence ($\phi\ \theta\ \psi$), relating the initial attitude of $\boldsymbol{F}^{ium}$ with $\boldsymbol{F}^{g}$, which is derived as follows (Diebel 2006):

$$\begin{bmatrix}\phi\\ \theta\\ \psi\end{bmatrix} = \begin{bmatrix}\text{atan2}(r_2, r_3)\\ -\text{asin}(r_1)\\ 0\end{bmatrix} \quad \textbf{(17)}$$

where the definition of the four quadrant inverse tangent function is:

$$\text{atan2}(y,x) = \begin{cases}\text{atan}(y/x) & if \quad x > 0\\ \text{atan}(y/x) - \pi & if \quad x < 0 \wedge y < 0\\ \text{atan}(y/x) + \pi & if \quad x < 0 \wedge y > 0\end{cases} \quad \textbf{(18)}$$

With the Euler angle triplets in Eq. (17), the initial quaternion, indicated by *n*=0 in Eq. (19), and its corresponding rotation matrix can be calculated based on quaternion algebra theories (Kuipers 1999; Diebel 2006):

$$\mathbf{q}_{n=0} = \begin{bmatrix} c_{\phi/2}c_{\theta/2}c_{\psi/2} + s_{\phi/2}s_{\theta/2}s_{\psi/2}\\ -c_{\phi/2}c_{\theta/2}c_{\psi/2} + s_{\phi/2}c_{\theta/2}c_{\psi/2}\\ c_{\phi/2}s_{\theta/2}c_{\psi/2} + s_{\phi/2}c_{\theta/2}s_{\psi/2}\\ c_{\phi/2}c_{\theta/2}s_{\psi/2} - s_{\phi/2}s_{\theta/2}c_{\psi/2}\end{bmatrix} \quad \textbf{(19)}$$

$$R_i^g(\mathbf{q}_{n=0}) = \begin{bmatrix} q_{n,0}^2 + q_{n,1}^2 - q_{n,2}^2 - q_{n,3}^2 & 2(q_{n,1}q_{n,2} - q_{n,0}q_{n,3}) & 2(q_{n,1}q_{n,3} + q_{n,0}q_{n,2})\\ 2(q_{n,1}q_{n,2} + q_{n,0}q_{n,3}) & q_{n,0}^2 - q_{n,1}^2 + q_{n,2}^2 - q_{n,3}^2 & 2(q_{n,2}q_{n,3} + q_{n,0}q_{n,1})\\ 2(q_{n,1}q_{n,3} + q_{n,0}q_{n,2}) & 2(q_{n,2}q_{n,3} + q_{n,0}q_{n,1}) & q_{n,0}^2 - q_{n,1}^2 - q_{n,2}^2 + q_{n,3}^2\end{bmatrix} \quad \textbf{(20)}$$

where *c* and *s* are simplified expression of *cos* and *sin* functions. The subscript $n = 0$ indicates the initial quaternion calculation. For instantaneous rotation matrices explained in the next section, $n = 1,2,\cdots k$.

It is worth mentioning that the yaw angle ψ is set to zero because only a vertical reference vector (gravity reactive force) is used for the initial orientation calculation. To correct the yaw angle, the environmental magnetism was usedand calibrated as shown in Figure 21. The IMU is placed on a 4 feet tall wood stand and aligned such that its coordinate frame is coincident with

the predefined global coordinate frame. Then the magnetometer's reading determines the angle α between X_g and the horizontal component of the environmental magnetism, M_h.

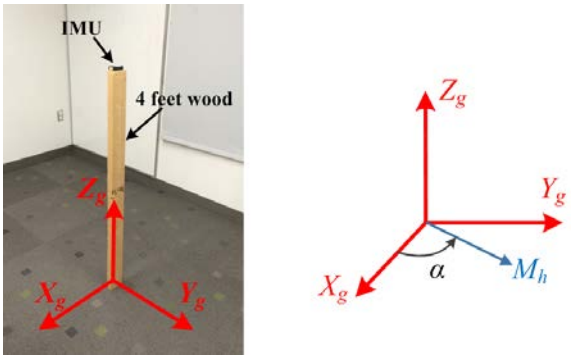

(a) Environmental magnetism calibration (b) heading angle compensation

Figure 21 Initial heading angle calculation

Assume the magnetometer's reading at the arbitrary stationary period is $\boldsymbol{M}_{stat}$. Apply the rotation matrix obtained in Eq. (20) on $\boldsymbol{M}_{stat}$, and take the first two elements to get its horizontal component M_h' as in Eq. (21):

$$M_h' = \boldsymbol{e}_{12} \cdot \left(R_i^g(\mathbf{q}_{n=0}) \cdot \boldsymbol{M}_{stat}\right) \quad \textbf{(21)}$$

where $\boldsymbol{e}_{12}$ is the operational matrix to take the first two components of $\boldsymbol{M}_{stat}$,

$$\boldsymbol{e}_{12} = \begin{bmatrix} 1 & 0 & 0 \\ 0 & 1 & 0 \end{bmatrix} \quad \textbf{(22)}$$

Assume the counterclockwise angle from M_h to M_h' is α', then the yaw angle is corrected to be:

$$\psi = \alpha + \alpha' \quad \textbf{(23)}$$

And then plug the newly updated yaw angle into Eq. (19) and (20) to get the fully determined initial quaternion and rotation matrix.

3.4.2 Instantaneous rotation matrix

After the initial quaternion is determined, the instantaneous quaternion will be changing while the IMU is undergoing arbitrary rotations. The function for updating the instantaneous quaternion is given by Eq. (24):

$$\frac{d}{dt}\mathbf{q} = \frac{1}{2}\Omega\left[\boldsymbol{\omega}^i\right] \cdot \mathbf{q} \qquad (24)$$

where the 4×4 matrix $\Omega\left[\boldsymbol{\omega}^i\right]$ is constructed by $\boldsymbol{\omega}^i$: the angular velocity vector expressed with respect to the IMU coordinate frame, i.e. the output of the gyroscope. Detailed mathematical derivation can be found in (Kuipers 1999; Diebel 2006).

$$\Omega\left[\boldsymbol{\omega}^i\right] = \begin{bmatrix} 0 & -\omega_x & -\omega_y & -\omega_z \\ \omega_x & 0 & \omega_z & -\omega_y \\ \omega_y & -\omega_z & 0 & \omega_x \\ \omega_z & \omega_y & -\omega_x & 0 \end{bmatrix} \qquad (25)$$

This updating process will possibly deviate the quaternion from its unity norm. A practical manipulation in (Sabatini 2006; Wang, Hsu et al. 2010) has been applied in this work, i.e. at every step, the updated quaternion will is forced to be normalized to unity:

$$\mathbf{q}_n^+ = \frac{\mathbf{q}_n^-}{\|\mathbf{q}_n^-\|} \qquad (26)$$

where the superscript (-) represents the result calculated by Eq. (26) at time step *n*, and (+) means the normalized quaternion which will be applied for the following steps and rotation matrix calculation. Since the quaternion at every sample moment is available, the instantaneous rotation matrix can be determined by Eq. (20).

3.5 CHAPTER SUMMARY

This chapter has established the essential theoretical fundamentals of the coordinate frame flow chart towards the coordinate frame transformation problem involved in multi-IMU application. On the basis of this newly developed method, the CFC of the two-segment throwing arm, as well as the associated coordinate frame transforms have been built. Some of the transformations were directly obtained by the alignment procedure (3.3) and the instantaneous rotation matrix updating procedure (3.4). Some of the indirect transforms were formed by superposition of multiple direct transforms suggested by the CFC.

The CFC can be systematically expanded to involve more coordinate frames to analyze even whole body movement and different types of motions. On the basis of the rotation matrices obtained in this chapter, anatomical arm rotations will be explained in detail in the next chapter.

4.0 UPPER EXTREMITY KINEMATIC ANALYSIS FOR THROWING

Overhead throwing is a representative kinematic chain motion involving all body segments from the feet to the hand. Theoretically, multiple IMUs must be placed on all of these body segments to get the complete kinematic chain motion. In order to keep the work in a compact form while still delivering enough necessary information regarding reconstruction of the kinematic chain, only throwing arm kinematics and dynamics are studied in this work by using two IMUs. The motion analysis procedures developed in the following chapters can later be extended to whole body kinematic or kinetic study without much modification. This chapter focuses on kinematics analysis and is divided into two sections. Section 4.1 explains how to reconstruct the trajectory of the throwing arm for spatial analysis of the kinematic chain while section 4.2 focuses on quantitatively analyzing the timing of arm segment rotations, which could be a useful tool for temporal analysis of the kinematic chain. Experimental validation is also carried out and results for each study will be addressed in respective sections. Section 4.3 briefly summarizes this chapter.

4.1 UPPER EXTREMITY TRAJECTORY RECONSTRUCTION

4.1.1 Theory and method

During the throwing motion, the accelerometer undergoes a combination of gravitational acceleration and the IMU's own linear acceleration. This combined acceleration projects to the IMU's coordinate frame whose orientation is changing all the time. With the initial and instantaneous rotation matrices obtained in section 3.4, the expression of accelerometer output can be transformed into $\boldsymbol{F}^{g}$. Thus, the gravitational acceleration can be removed to get the IMU's acceleration:

$$\boldsymbol{a}_{ium}^{g} = R_{ium}^{g} \cdot \boldsymbol{a}_{ium}^{ium} - \boldsymbol{GR}^{g} \quad (27)$$

$$\boldsymbol{GR}^{g} = [0 \quad 0 \quad |g|]^{T} \quad (28)$$

where $\boldsymbol{a}_{ium}^{ium}$ is the output of the accelerometer, i.e. acceleration of the IMU on upper arm (indicated by subscript *ium*) expressed in the IMU frame (indicated by the superscript *ium*). The coordinate frame transform operation (indicated by R_{ium}^{g}) will transform the expression from $\boldsymbol{F}^{ium}$ into $\boldsymbol{F}^{g}$. $\boldsymbol{GR}^{g}$ is the gravitational reaction acceleration expressed in $\boldsymbol{F}^{g}$. The integration of $\boldsymbol{a}_{ium}^{g}$ with respect to time leads to velocity and trajectory of the IMU observed in the global frame:

$$\boldsymbol{v}_{ium}^{g} = \int \boldsymbol{a}_{ium}^{g} \cdot dt \quad (29)$$

$$\boldsymbol{s}_{ium}^{g} = \iint \boldsymbol{a}_{ium}^{g} \cdot dt^{2} \quad (30)$$

The kinematics of the IMU on the forearm can be obtained by the same way demonstrated by Eqs (27) to (30).

Since the arm segments are assumed to be rigid bodies, the trajectory of the arm can be reconstructed on the basis of the position of the IMU and the attitude of the arm segment in $\boldsymbol{F}^g$. The position vector of the proximal end (shoulder) and distal end (elbow) relative to the IMU can be written as three element column vectors in the upper arm coordinate system, and likewise the position vector of the elbow can be written as a vector in the forearm coordinate system:

$$\boldsymbol{l}_{sd/ium}^{um} = [0 \quad 0 \quad l_1]^T \tag{31}$$

$$\boldsymbol{l}_{eb/ium}^{um} = [0 \quad 0 \quad -l_2]^T \tag{32}$$

$$\boldsymbol{l}_{eb/ifm}^{fm} = [0 \quad 0 \quad l_3]^T \tag{33}$$

where l_1, l_2 and l_3 are scale values measured as soon as the IMUs are deployed on subject's arm from the geometric center of sensors to bony locations. According to the coordinate directions defined in Figure 18, positive or negative signs are assigned appropriately.

To transform these position vectors from $\boldsymbol{F}^{um}$ and $\boldsymbol{F}^{fm}$ to $\boldsymbol{F}^g$, the indirect coordinate frame transform is constructed as shown in Figure 22.

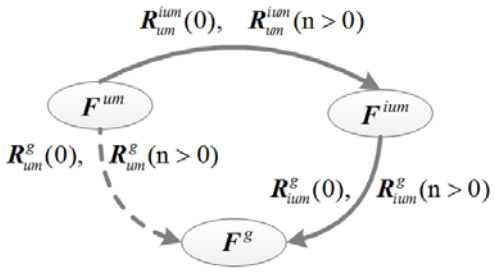

Figure 22 Indirect transform from upper arm frame to global frame

Then, the position vectors in $\boldsymbol{F}^g$ can be determined:

$$\boldsymbol{s}_{sd}^{g} = R_{um}^{g} \cdot \boldsymbol{l}_{sd/ium}^{um} + \boldsymbol{s}_{ium}^{g} \tag{34}$$

$$\boldsymbol{s}_{eb(um)}^{g} = R_{um}^{g} \cdot \boldsymbol{l}_{eb/ium}^{um} + \boldsymbol{s}_{ium}^{g} \tag{35}$$

$$\boldsymbol{s}_{eb(fm)}^{g} = R_{fm}^{g} \cdot \boldsymbol{l}_{eb/ifm}^{fm} + \boldsymbol{s}_{ifm}^{g} \quad (36)$$

$$\boldsymbol{s}_{wt}^{g} = \boldsymbol{s}_{ifm}^{g} \quad (37)$$

Eqs. (35) to (37) will be calculated for every sample time instant, although (*t*) is omitted in parameter expression. The location of IMU on the forearm (*ifm*) is very close to the wrist, thus the position vector of the wrist ($\boldsymbol{s}_{wt}^{g}$) is considered to be equivalent to that of the IMU on the forearm ($\boldsymbol{s}_{ifm}^{g}$) as shown in Eq. (37). Due to various error sources existing in the sensor, measurement and calculation, the elbow position calculated by the two methods, Eqs. (35) and (36), may have different results. However, the anatomical constraint does not allow any 'break' of the joint, so the corrected elbow position is obtained by:

$$\boldsymbol{s}_{eb}^{g} = w \cdot \boldsymbol{s}_{eb(um)}^{g} + (1 - w) \cdot \boldsymbol{s}_{eb(fm)}^{g} \quad (38)$$

where w and $(1 - w)$ are weight factors that express the reliability of the results calculated by Eqs. (35) and (36) respectively. In this work, the two IMUs are assumed to accumulate same amount of error. Thus, $w = 0.5$ is used for elbow trajectory correction.

4.1.2 Results and application example

Two IMUs were firmly placed on the throwing arm by elastic bands and medical tape as shown in Figure 13. The measurement specification of the IMUs in use is listed in Table 3. The IMUs are calibrated as explained in Appendix A.

The IMU alignment procedure was performed to obtain the alignment matrices, as explained in section 3.3. As mentioned in A.2.1, the bias of the gyroscope was calibrated before every trial. Taking account of the fact that the output of the gyroscope while stationary is actually zero angular velocity, the subject was asked to stand still at rest posture for 5 seconds which allowed

the gyroscope to record zero velocity output. Meanwhile, during this period, the accelerometer was measuring gravity and magnetometer was measuring pre-calibrated environmental magnetic field. These sensor outputs are used for initial attitude calculation. After this 5 second stationary period, the subject was asked to throw a foam ball at a low level of exertion which ensured that the motion would not saturate the inertial sensors (in particular the angular rate gyros).

Table 3 Manufacturer specification of the IMU.

Sensor type	Range	Sensitivity
Accelerometer	±24(g)	0.012 (g/digit)
Gyroscope	±2,000 (°/sec)	0.07 (°/sec/digit)
Magnetometer	1.3 (Ga)	5 (mGa/digit)

The procedures are summarized as follows:

Step 1: System calibration and initialization: the IMUs were calibrated following the calibration protocol explained in 0;

Step 2: Sensor deployment: two IMUs were attached on the upper arm and the forearm respectively;

Step 3: IMU alignment: the subject was asked to stand still with throwing arm at anatomical neutral posture for 5 seconds, then perform shoulder flexion/extension with elbow fully extended in sagittal plane for 5 repetitions. More details can be found in section 3.3;

Step 4: Throwing motion: the subject was asked to hold a foam ball stationary for 5 seconds, then throw the ball towards the target using baseball pitching technique but at low level of exertion.

The flow chart of the data processing algorithm for reconstructing the IMU and arm trajectories is shown in Figure 23. In this flow chart, ellipse shapes indicate data sets while rectangular shapes stand for subroutines of the data processing algorithm.

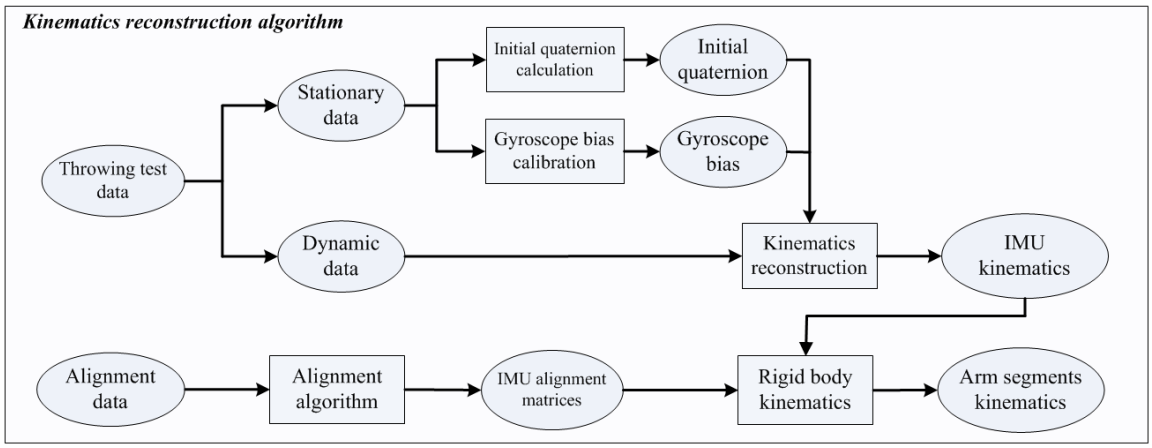

Figure 23 Flow chart of the kinematics reconstruction algorithm

In Figure 23, [Alignment algorithm] consists of Eq. (10) to (13) explained in section 3.3. The <throwing test data> is divided into <stationary data> and <dynamic data>. The <stationary data> goes through the [initial quaternion calculation] algorithm demonstrated by Eqs. (16) to (23), while the <dynamic data> as well as <initial quaternion> and <gyroscope bias> is processed by the instantaneous [kinematics reconstruction] procedure shown by Eqs. (24) to (26) and (30). The [rigid body kinematics] algorithm rebuilds the arm segment kinematics based on results obtained above. The algorithm software and data processing procedure has been programmed and tested in Matlab (Inc. 2012).

Results of arm segment trajectory reconstructed by IMU data are shown in Figure 24. The series of red and blue lines represent position of the upper arm and forearm, respectively, at each sample time instant. The point of view is defined as follows: the subject stands with left shoulder (right hand thrower) towards the target, and faces the observer. Thus, the view from the observer is side view, and the view towards the target is the back view. The start point can be identified

from the side view plot. The elbow starts at the (0, 0) position where the upper arm and forearm create an angle in front of the body with the hands together (the so-called “set position” for a pitcher), which is also the ready posture of the subject. The two black lines represent trajectories of the IMUs. However, before application of the anatomical constraint, the error and inaccurate anatomy measurement cause mismatch of $\boldsymbol{s}^{g}_{eb(um)}$ and $\boldsymbol{s}^{g}_{eb(fm)}$. This error is obvious in Figure 24, as the forearm and upper arm are disconnected at each sample moment, which can be identified by the gap between blue lines and red lines. After applying the anatomical constraint, the corrected arm trajectory plot is shown in Figure 25.

With this arm trajectory plot, coaches or players are able to visually identify the throwing mechanics, and can use that information to make decisions for improvements. As shown in Figure 26, different stages of throwing motion can be identified from the arm trajectory, however, the transition from one stage to the next is somewhat subjective and, with the exception of quantitative information, the arm trajectory plot is essentially the same as analyzing high-speed video. Because IMU hardware is potentially able to sample at over 1,000 Hz, the data allows coaches or players to see small details of arm motion. It will be shown in the following sections that the IMU-based data can provide much more insight into the throwing motion than simply arm trajectory.

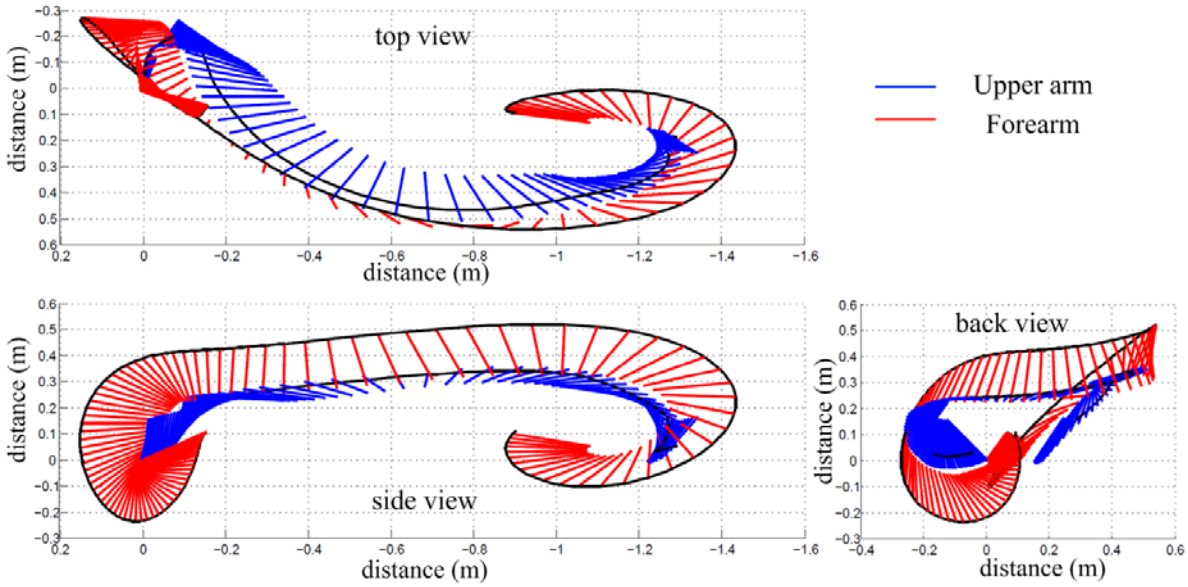

Figure 24 Arm trajectory reconstruction without anatomical constraint

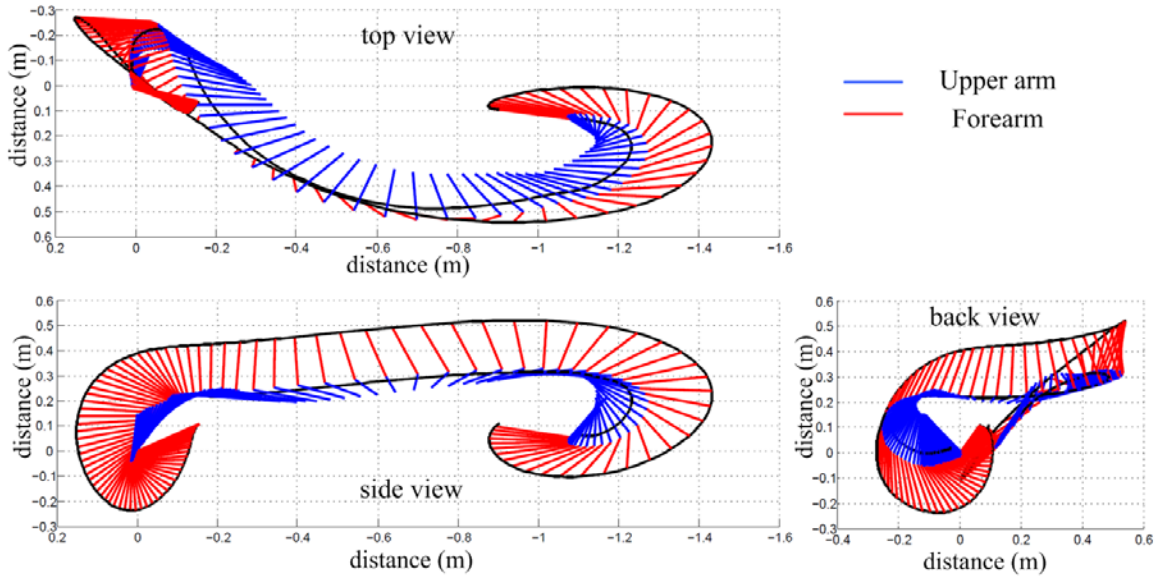

Figure 25 **Arm trajectory reconstruction with anatomical constraint**

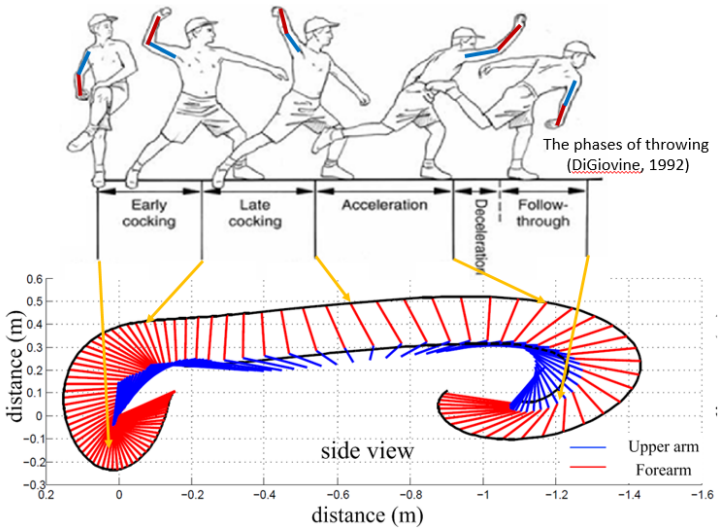

Figure 26 Visual identification of throwing mechanics based on trajectory plot

4.1.3 Experimental validation with video camera based motion capture system

In this section, a validation experiment is designed in order to validate the functionality of the system for trajectory reconstruction of the overhead throwing motion. The experimental setup is shown in Figure 27. The Vicon motion capture system was applied to provide reference motion data for validation purposes. A set of reflective markers were attached at body landmarks on the subject. While the subject performed throwing motions, the two systems captured and recorded kinematics data simultaneously. To be more specific, the Vicon system recorded position data of those reflective markers while IMUs collected acceleration and angular velocity data of arm segments. The Vicon system was calibrated to 1 mm accuracy for location data, which was accurate enough for validating the kinematics reconstruction system designed in this work. The test lab, video camera based motion capture system as well as its data processing were provided by Human Movement & Balance Laboratory of University of Pittsburgh. All of the experiment protocol design, test procedure and data processing have been reviewed and approved by

Institutional Review Board of the University of Pittsburgh. Consent was obtained from each test subject prior to participation in the test. Test data and any privacy information were all saved in secured lab computer in University of Pittsburgh with authorized access and password.

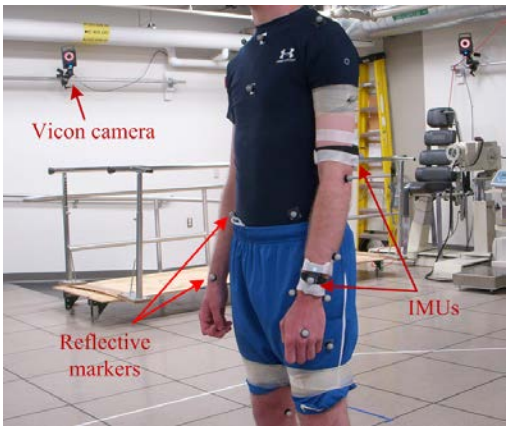

Figure 27 Validation experiment setup

The trajectory calculated by the IMU data was compared to the location data recorded by the markers attached on the two IMUs. The trajectory comparison breaks down into three axes, as shown in Figure 28. The three plots on left column are show the comparison of the IMU and marker deployed on the forearm, while the right column shows the comparison of the upper arm IMU and its marker.

The difference between the two sets of results is quantified in **Table 4**. RMSE represents the root mean square error between the two trajectories under comparison, shown as Eq. (39),

$$RMSE = \sqrt{\frac{1}{N}\sum_{k=1}^{N}\left(S_m(k) - \widehat{S}_\iota(k)\right)^2} \quad \textbf{(39)}$$

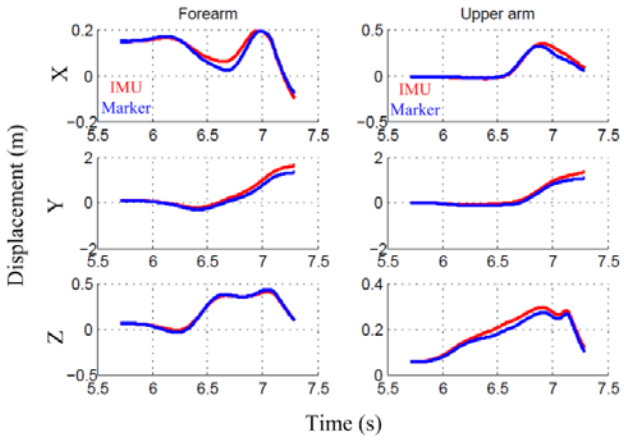

Figure 28 Displacement comparison between IMU and Vicon marker

Because the Vicon system and the IMU system are recording data at different start moments and different sampling frequencies, the Vicon system's sample time series will be used as reference for interpolating IMU's data. In Eq. (39), $\boldsymbol{S_m(k)}$ is the position of the markers at sample time instant *k*, while $\boldsymbol{\widehat{S}_i(k)}$ is the position calculated by the IMU data and interpolated into sample time instant *k* which is same as that of Vicon system result. The RMSE is divided by the motion range on each respective axis to produce % of RMSE:

$$\%\ of\ RMSE = \frac{RMSE_i}{\left|S_{m,i,max} - S_{m,i,min}\right|} \qquad \textbf{(40)}$$

where $S_{m,i,max}$ and $S_{m,i,min}$ are maximum and minimum marker positions for axis *i*, so that $\left|S_{m,i,max} - S_{m,i,min}\right|$ is the travel range of the marker on axis *i*. $RMSE_i$ is calculated by Eq. (39) for a specific axis. The correlation coefficient shown in the last column of Table 5 indicates the similarity of the two trajectories.

In Table 4, it is indicated that using the IMUs for kinematics reconstruction is a feasible approach. The IMU hardware specification limited the accuracy level in this work, which is, however, still good enough for system validation purposes. The IMUs are working at 250 Hz in

this work due to hardware limits. If a higher sampling frequency is achieved by using better design of sensor hardware, more accurate results can be obtained in future work.

Table 4 Trajectory comparison results of Vicon system and IMU system

	Axis	RMSE (m)	% of RMSE	Correlation coefficient
Forearm IMU	*X*	0.0191	6.37%	0.965
	Y	0.1434	7.15%	0.996
	Z	0.0132	2.64%	0.999
Upper arm IMU	*X*	0.0272	6.8%	0.989
	Y	0.1043	6.52%	0.997
	Z	0.0184	6.13%	0.997

Note 1: The validation was carried out based on the comparison between IMU trajectory calculated by IMU itself and a video camera system. The specific anatomical bony landmark trajectory, e.g. trajectory of the shoulder, was not evaluated. The reasons are: from the Eqs. (34) to (37), the accuracy of bony landmark trajectory reconstruction depends on the accuracy of the IMU's trajectory, arm segment attitude and position vector, for example $\boldsymbol{s}_{ium}^{g}$, R_{um}^{g} and $\boldsymbol{l}_{sd/ium}^{um}$ respectively in Eq. (34). Since the arm segments have uneven and changeable skin surface during motion, the accurate anatomical measurement, $\boldsymbol{l}_{sd/ium}^{um}$, is very hard to achieve. The direct comparison of anatomical spot trajectory will contain unpredictable error in $\boldsymbol{l}_{sd/ium}^{um}$, which will degrade the functionality and accuracy of the algorithm designed in this work. Thus this section has validated IMU's trajectory calculation accuracy, and the arm segment attitude calculation is implicitly validated by the following arm rotation velocity validation. Thus, the anatomical segment trajectory accuracy will not be evaluated explicitly here. It is worth mentioning that if a redundant IMU network is applied to a single body segment, as well as application of some anatomical constraint, a better anatomical location measurement could be achieved.

Note 2: Multiple trials were taken in the experiment validation. However, many trials showed large amount of difference between the IMU calculated trajectory and video camera captured trajectory. A close investigation showed this issue was due to the inertial sensor hardware limitation. All three sensor chips, accelerometer, gyroscope and magnetometer, are enable to record data. At the 250Hz frequency, these particular inertial sensors lose data frequently. If the data loss happened during key the dynamic period of the test (particularly the acceleration stage of the throw), the integration process of the algorithm would have large deviation from the true trajectory. Thus, statistical analysis on the trials that includes this data cannot present a fair evaluation of the algorithm. The best case is presented here to demonstrate the feasibility of the algorithm.

4.2 UPPER EXTREMITY ROTATIONS RECONSTRUCTION

4.2.1 Theory and method

The upper extremity rotations being investigated in this work are upper arm internal and external rotation, elbow flexion and extension, and forearm pronation and supination. For simplification, these terms will be annotated as upper arm IN/EX, elbow FX/ES, and forearm PN/SN. The graphical demonstration of the three upper extremity rotations is shown in Figure 29.

During the process of a typical overhead throwing motion, the acceleration stage is mainly made up of by upper arm internal rotation, elbow extension, and forearm pronation. For this reason, these three directions are defined as positive, while their counterparts are negative. The detailed explanation of the upper extremity rotations is as follows:

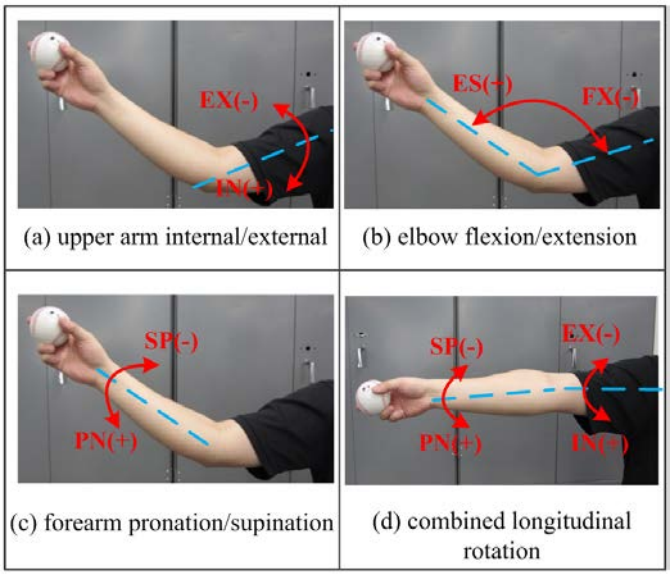

Figure 29 Demonstration of arm rotations under reconstruction.

(a) Upper arm IN/EX: the rotation of the upper arm along its longitudinal axis, which is Z_{um} as defined in section 3.1. The direction is defined as positive ($+Z_{um}$) while rotating internally, and negative while rotating externally ($-Z_{um}$) ;

(b) Elbow flexion/extension: for the purpose of simplification and ease in calculation, this rotation is represented by change of the angle between the two longitudinal axes of upper arm (Z_{um}) and forearm (Z_{fm}), the direction is defined as positive for extension (+), and negative for flexion (-);

(c) Forearm pronation/supination: the rotation of the forearm along its longitudinal axis, which is Z_{fm} as defined in section 3.1. The direction is defined as positive for pronation ($+Z_{fm}$) and negative for supination ($-Z_{fm}$).

Upper arm IN/EX:

The upper arm is connected to its proximal segment, i.e. upper torso. The measured angular velocity by IMU attached on the upper arm is the absolute rotation velocity of the upper arm which is superposition of the upper torso rotation and the upper arm rotation about its own anatomical axes. Thus, the proximal segment rotation must be subtracted from the IMU measurement. In this work, only two IMUs are deployed on arm segments, thus the upper torso rotation is neglected for simplification. Because the upper torso rotation is much slower than the upper arm, this assumption will not introduce significant error in calculation results. If a third IMU is applied and attached at the position of the scapula, the upper torso rotation can be subtracted to get better results.

In order to calculate the anatomical rotation of upper arm, the physical quantities should be transformed into $\boldsymbol{F}^{um}$. The CFC of this rotation is established as shown in Figure 30. Then the equation to calculate the upper arm IN/EX is:

$$\boldsymbol{\omega}_{um}^{um}(t) = \boldsymbol{k} \cdot \left(R_{ium}^{um}(t) \cdot \boldsymbol{\omega}_{ium}^{ium}(t) \right) \quad \textbf{(41)}$$

$$\omega_{IN/EX}(t) = \boldsymbol{e}_3^T \cdot \boldsymbol{\omega}_{um}^{um}(t) \quad \textbf{(42)}$$

where $\boldsymbol{\omega}_{ium}^{ium}(t)$ is angular velocity captured by the gyroscope deployed on the upper arm, it is a 3×1 vector and expressed in coordinates of $\boldsymbol{F}^{ium}$. The rotation matrix $R_{ium}^{um}(t)$ transforms the gyroscope output into upper arm frame $\boldsymbol{F}^{um}$ at every sample instant, which is anatomical rotation rate. $\boldsymbol{e}_3^T = [0 \quad 0 \quad 1]$ is an operational vector taking the third element from the upper arm rotation velocity vector. With the assumption that the inertial/external rotation velocity is linearly distributed on the forearm, which means the proximal side of forearm has zero velocity of internal/external rotation while the distal side has the largest value. Since the IMU on the

forearm is not strictly attached on the distal side, a linear interpolation correction factor *k* is used to get upper arm IN/EX:

$$\boldsymbol{k} = \begin{bmatrix} 1 & 0 & 0 \\ 0 & 1 & 0 \\ 0 & 0 & \dfrac{l_{um}}{l_{ium/sd}} \end{bmatrix} \quad \textbf{(43)}$$

where l_{um} is the length of the forearm while $l_{ium/sd}$ is the distance from IMU on upper arm to the shoulder.

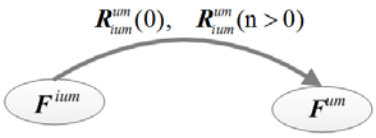

Figure 30 CFC for upper arm IN/EX calculation

Elbow FX/ES:

The elbow FX/ES angle is defined as the angle between the longitudinal axes of the forearm and the upper arm. Define the directional vector of the two longitudinal axes in their own coordinate frames, $\boldsymbol{e}_{d_{um}}^{um}$ and $\boldsymbol{e}_{d_{fm}}^{fm}$:

$$\boldsymbol{e}_{d_{um}}^{um} = ([0 \quad 0 \quad 1]^T)^{um} \quad \textbf{(44)}$$

$$\boldsymbol{e}_{d_{fm}}^{fm} = ([0 \quad 0 \quad -1]^T)^{fm} \quad \textbf{(45)}$$

These two directional vectors are constant while expressed in their own frames. However, mathematically, in order to calculate the angle between the two attitude vectors, they must be expressed in the same frame $\boldsymbol{F}^g$. From the CFC shown in Figure 31, the upper arm attitude vector will go through the transform: $\boldsymbol{F}^{um} \rightarrow \boldsymbol{F}^{ium} \rightarrow \boldsymbol{F}^g$ while the forearm attitude vector will go through the transform: $\boldsymbol{F}^{fm} \rightarrow \boldsymbol{F}^{ifm} \rightarrow \boldsymbol{F}^g$.

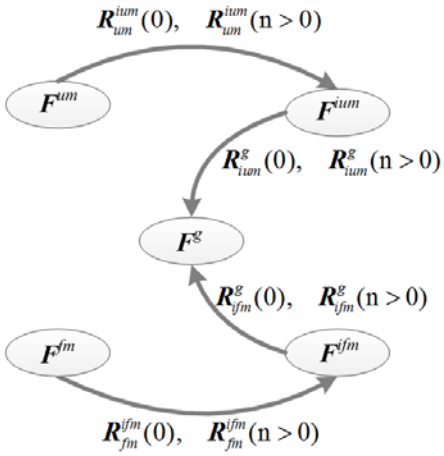

Figure 31 CFC for elbow FX/ES calculation

The corresponding equations are:

$$\boldsymbol{e}_{d_{um}}^{g} = R_{ium}^{g}(t) \cdot R_{um}^{ium}(t) \cdot \boldsymbol{e}_{d_{um}}^{um} \quad \textbf{(46)}$$

$$\boldsymbol{e}_{d_{fm}}^{g} = R_{ifm}^{g}(t) \cdot R_{fm}^{ifm}(t) \cdot \boldsymbol{e}_{d_{fm}}^{fm} \quad \textbf{(47)}$$

at every sample time instant the angle between the upper arm and forearm is

$$\beta(t) = \arccos\left(\frac{\boldsymbol{e}_{d_{um}}^{g}(t) \cdot \boldsymbol{e}_{d_{fm}}^{g}(t)}{\left|\boldsymbol{e}_{d_{um}}^{g}(t)\right| \cdot \left|\boldsymbol{e}_{d_{fm}}^{g}(t)\right|}\right) \quad \textbf{(48)}$$

and the angular velocity of the elbow FX/ES is:

$$\omega_{FX/ES}(t) = \frac{d}{dt}\big(\beta(t)\big) \quad \textbf{(49)}$$

Forearm PN/SN:

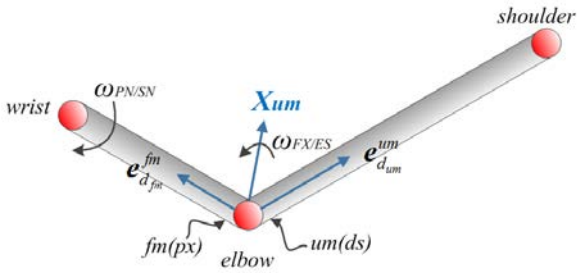

Figure 32 Demonstration of elbow flexion/extension and forearm pronation/supination

Assume the elbow is a hinge joint, which means the forearm is restricted to the plane defined by Y_{um} and Z_{um}. The rotation velocity at the proximal end of the forearm (labeled as *fm(px)*) is the superposition of upper arm rotation and elbow FX/ES which is also the relative rotation of the *fm(px)* to distal end of the upper arm (abbreviated as *um(ds)*).

$$\boldsymbol{\omega}_{fm(px)}^{fm} = R_{um}^{fm} \cdot \left(\boldsymbol{\omega}_{um}^{um} + \boldsymbol{\omega}_{FX/ES}^{um}\right) \quad (50)$$

where $\boldsymbol{\omega}_{FX/ES}^{um}$ is the vector form of the elbow FX/ES expressed in $\boldsymbol{F}^{um}$, with the value of the elbow FX/ES and calculated by:

$$\boldsymbol{\omega}_{FX/ES}^{um} = [\omega_{FX/ES} \quad 0 \quad 0]^T \quad (51)$$

$\boldsymbol{\omega}_{um}^{um}$ is the angular velocity of the upper arm expressed in $\boldsymbol{F}^{um}$ and implicitly calculated by Eq. (43). The remaining term in Eq. (50) is the rotation matrix R_{um}^{fm}. Since there is no direct transform between $\boldsymbol{F}^{fm}$ and $\boldsymbol{F}^{um}$, an indirect transform is established as shown in the CFC as shown in Figure 33.

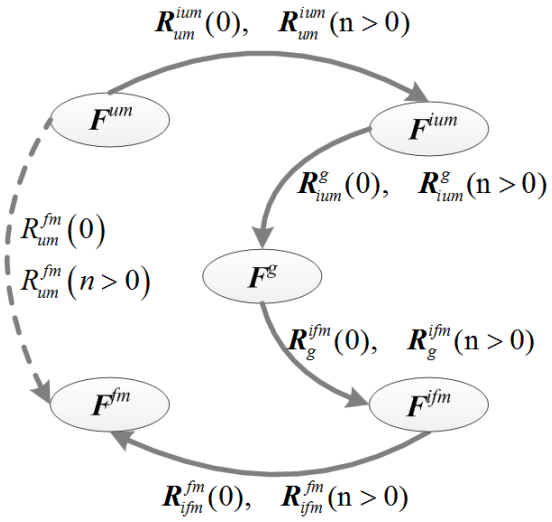

Figure 33 CFC of indirect transform from upper arm to forearm

The indirect coordinates frame transform from $\boldsymbol{F}^{um}$ to $\boldsymbol{F}^{fm}$ is established as:

$$\boldsymbol{F}^{um} \rightarrow \boldsymbol{F}^{fm} = \boldsymbol{F}^{um} \rightarrow \boldsymbol{F}^{ium} \rightarrow \boldsymbol{F}^{g} \rightarrow \boldsymbol{F}^{ifm} \rightarrow \boldsymbol{F}^{fm} \quad \textbf{(52)}$$

and the forearm PN/SN rotation is obtained by:

$$\omega_{PN/SN}(t) = \boldsymbol{e}_3^T \cdot \left(R_{ifm}^{fm}(t) \cdot \boldsymbol{\omega}_{ifm}^{ifm}(t) - \boldsymbol{\omega}_{fm(px)}^{fm}(t) \right) \quad \textbf{(53)}$$

4.2.2 Experiment validation with video camera based motion capture system

The Vicon motion capture system setup is the same as that explained in Section 4.1.2. Since the throwing motion is a complex combination of multiple rotations, a simple experiment routine is designed to validate the feasibility of the IMU system in reconstructing the anatomical rotations explained in previous sections. During the test, the subject went through the following test procedure (detailed protocol includes warm up, calibration and so forth, which is not listed here; each step can be carried out at any general arm orientation, unless otherwise specified):

a) Forearm PN/SN: keeping the upper arm still, rotate the forearm along the longitudinal axis to carry out the pronation/supination twice as shown in Figure 29 (c);

b) Upper arm IN/EX: rotate the upper arm along the longitudinal axis to carry out the internal/external rotation twice, as shown in Figure 29 (a);

c) Elbow FX/ES: flex and extend the elbow to carry out the elbow extension/flexion twice, as shown in Figure 29 (b);

d) Combined rotation: fully extend the elbow, and rotate the upper arm and forearm along their longitudinal axis at the same time, as shown in Figure 29 (d).

Each subject completed each step listed above a total of 10 times, within which 5 cycles were performed at a slow speed (about 20% of subject's maximum capability) and 5 cycles were

performed at a fast speed (about 50% of subject's maximum capability). The slow speed and fast speed were subjectively controlled by the subjects, and were used in order to validate the system under a large range of rotation velocities. Figure 34 shows a group of example results of the angular velocity comparison between the multi-IMUs system (black solid line) and Body-Builder (BB) model of the Vicon motion capture system (red solid line).

As depicted in Figure 34, the general trend of the anatomical arm rotations calculated by the two methods match each other very well. It is clear that the multi-IMU system's results contain more high frequency motion information. This is because the marker location data has been passed through a low pass filter before numerical differentiation, which may exclude those high frequency components. The quantitative comparison results are listed in Table 5. For each subject, each arm rotation task was completed 10 times, which means a total 10 trials for each rotation were achieved. For example, subject 1 has 10 trials for forearm PN/SN, 10 trials for upper arm IN/EX, 10 trials for elbow FX/ES, and 10 trials for combined longitudinal rotation. The first column of data in Table 5 for each task shows the range of peak values for the particular measure. For instance, subject 1 completed 10 trials of forearm PN/SN, producing peak values of forearm rotational velocity ranging from 178 °/s to 635 °/s. The second column of data in Table 2 for each task presents the mean value (μ) and standard deviation (σ) of the normalized root mean square error (RMSE, comparing BB results to IMU results) for the total duration of the task.

The normalized RMSE is defined as the RMSE between the results of the two systems divided by the range of peak angular velocity values (from column 1), as shown in Eq. (54)

$$Normalized\ RMSE = \frac{\sqrt{\sum_{i=1}^{n}\left(v_i^{IMU} - v_i^{Vicon}\right)^2}}{v_{max}^{Vicon} - v_{min}^{Vicon}} \times 100\% \qquad \textbf{(54)}$$

where v_i^{IMU} is the angular velocity calculated by the multi-IMU system and interpolated in accordance with the sampling rate of v_i^{Vicon}, the angular velocity calculated by Vicon motion capture system.

Since the peak value of the rotation velocity is an important index of performance evaluation, and has even been related to injury (Bushnell, Anz et al. 2010; Hurd, Jazayeri et al. 2012), the difference between the peak values calculated by the two systems is also provided, which is calculated as:

$$peak\ value\ difference = \frac{v_{peak}^{IMU} - v_{peak}^{Vicon}}{v_{peak}^{Vicon}} \times 100\% \qquad \textbf{(55)}$$

There are 4 peaks within each trial, thus a total of 40 difference measures for peak value difference can be obtained for each rotation task. The mean value and standard deviation of the 40 numbers is listed below the normalized RMSE and placed in parentheses in Table 5. In summary, the normalized RMSE shows the averaged difference over the complete time history, and the peak value difference shows the most significant difference. The results in Table 5 indicate that there is large difference between the peak value calculations of the two systems. The worst case happened in the upper arm IN/EX rotation during combined motion of subject 3, which is 69.0±39.5%. Meanwhile the normalized RMES is 9.0±1.5%, which suggests that most of the difference occurred at the peak values.

Table 5 Normalized RMSE and peak value difference of angular velocity.

	Forearm PN/SN		Upper arm IN/EX		Elbow FX/ES		Forearm PN/SN in combined motion		Upper arm IN/EX in combined motion	
	Range (°/s)	μ ± σ (%)	Range (°/s)	μ ± σ (%)	Range (°/s)	μ ± σ (%)	Range (°/s)	μ ± σ (%)	Range (°/s)	μ ± σ (%)
Sub-01	178-635	4.1±0.5 (7.4±7.4)	25-445	12.4±5.6 (-23.9±11.0)	117-320	7.2±2.6 (6.6±7.3)	125-406	6.7±1.3 (5.9±10.9)	58-280	5.7±1.0 (28.5±31.8)
Sub-02	230-600	3.8±0.5 (16.6±14.5)	98-231	6.5±1.5 (7.8±9.5)	95-240	12.9±4.9 (20.1±40.7)	130-520	11.1±2.8 (12.9±23.7)	100-370	8.6±2.3 (54.9±53.0)
Sub-03	200-634	2.7±0.4 (4.3±6.2)	80-445	3.5±0.5 (9.8±10.3)	108-350	5.5±0.7 (11.5±3.5)	94-550	5.9±1.0 (43.6±11.6)	58-340	9.0±1.5 (69.0±39.5)

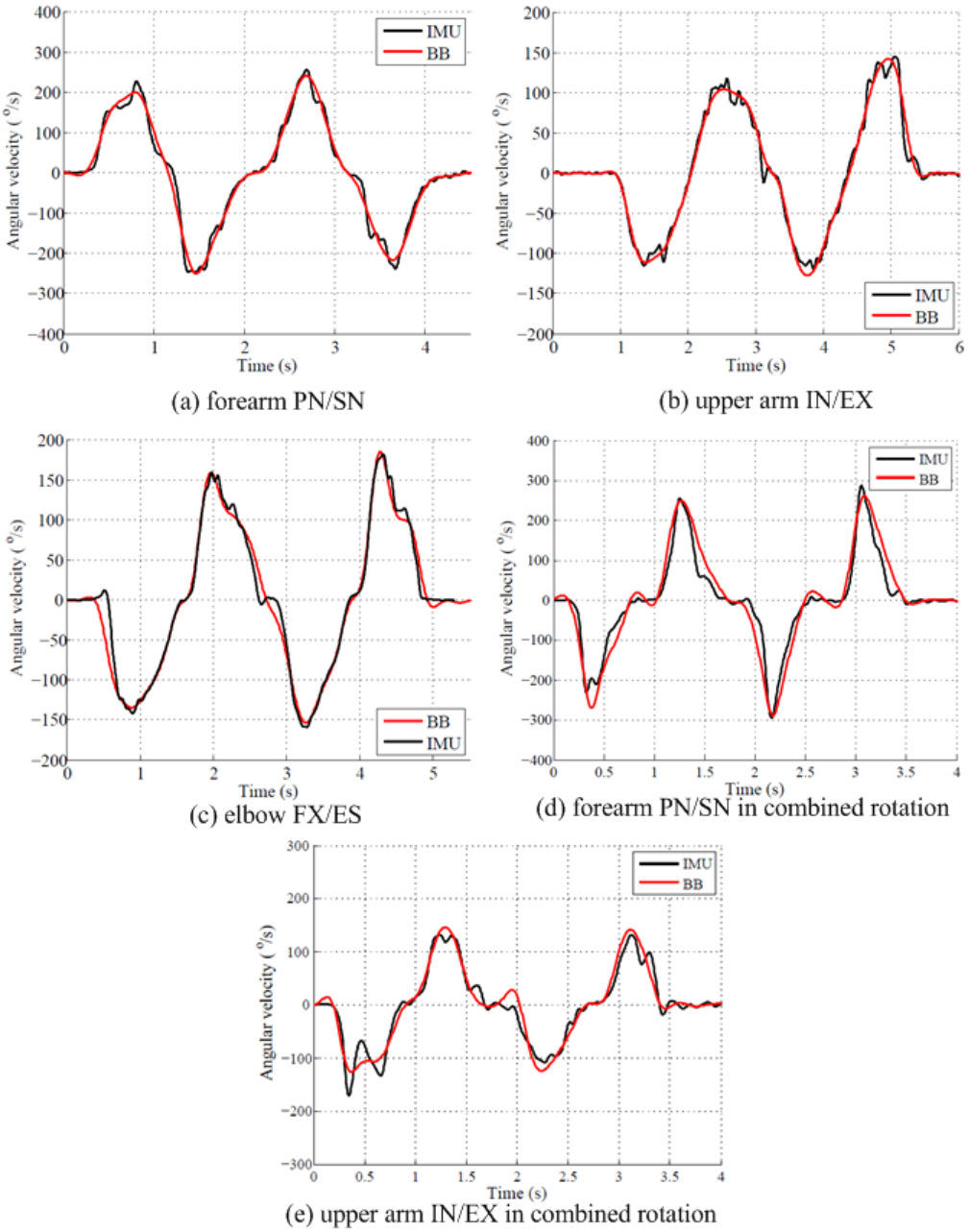

Figure 34 Anatomical arm rotation comparison

The anatomical rotation is identified by its direction or the sign of the velocity value. For instance, from the anatomical definitions of Figure 29(a), an angular velocity data point above zero in Figure 34(b) signifies upper arm internal rotation, while external rotation is indicated by a data point below zero. In this way, the kinematic chain timing is determined by the zero-crossings of the angular velocity plots. The mean values (μ) and standard deviations (σ) of the zero-crossing timing difference between the two systems are listed in Table 6.

Table 6 Angular velocity cross zero timing comparison

	Forearm PN/SN		Upper arm IN/EX		Elbow EX/FX		Forearm PN/SN in combined motion		Upper arm IN/EX in combined motion	
	μ (s)	σ (s)	μ (s)	σ (s)	μ (s)	σ (s)	μ (s)	σ (s)	μ (s)	σ (s)
Sub-01	-0.008	0.044	-0.004	0.033	-0.002	0.129	-0.002	0.065	-0.003	0.046
Sub-02	-0.007	0.026	-0.003	0.026	-0.013	0.029	-0.033	0.060	0.024	0.060
Sub-03	-0.009	0.034	-0.012	0.040	-0.006	0.091	0.0004	0.065	-0.04	0.081

Most of the cross zero timing difference is less than 0.01s, and is even smaller than the sampling interval of the Vicon motion capture system. The worst case, -0.04±0.081, happened at the upper arm IN/EX of combined motion of subject-03. The small difference between zero-crossing points demonstrates the feasibility of the multi-IMU system in kinematic chain timing reconstruction.

4.2.3 Experiment validation with single axis rotation rig

The validation results in the previous section illustrate the differences between the multi-IMU system developed in this work and video camera based motion capture system, especially at peak rotational velocities. The possible error sources could be due to the multi-IMUs, the Vicon motion capture system and even the subjects in the test. With regard to the multi-IMU system,

possible error sources include IMU calibration errors, sensor specification drift, misalignment between the IMU and anatomical frames, integration errors during the quaternion updating process, body measurement error and relative motion between IMUs and body segments. Potential errors associated with the video camera motion capture system include noise introduced by numerical differentiation, loss of sight of the markers, relative motion between markers and skin, as well as measurement error of bony landmarks. Because the arm segments are not strict rigid bodies, the rotation axes might not be constant. The amount of this inconsistency may vary from subject to subject, and thus deteriorate the accuracy of both the IMU algorithm and Vicon motion capture system. As a result, the comparison to the video camera motion capture system demonstrates the feasibility of the method developed in this paper, but is not able to make a fair judgment on the accuracy of the algorithm. It is of significant value to identify these error sources and investigate how they affect the accuracy of the two systems, e.g. IMU based system and video camera based system. Considering that the focus of this study is on developing the IMU-based anatomical rotation reconstruction algorithm and validating its feasibility and accuracy, a single axis rotation rig was designed to further investigate the accuracy of the algorithm itself by isolating other unknown error sources and eliminating their effects on the results.

As shown in Figure 35, the aluminum IMU holder can be rotated by the manual handle at arbitrary speed. The angular displacement is recorded by the optical encoder (5000 pulses/revolution) which is installed co-axial to the rotation axis, and considered as an accurate reference for validation purposes.

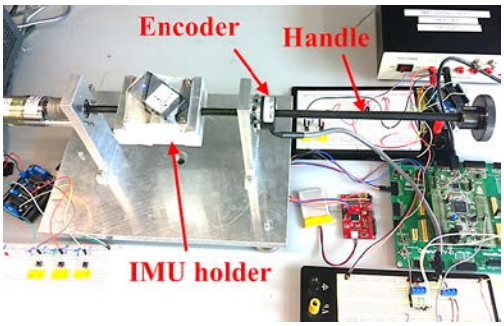

Figure 35 Experimental setup for single axis rotation rig validation.

Before the test, the IMU was attached to the holder firmly, similar to how it is attached to the forearm of during the human subject experiments. Without sacrificing generality, the IMU was arbitrarily attached to the holder and the alignment procedure introduced in section 3.3 was carried out to obtain the alignment matrix. In this setup, the IMU frame has the same meaning as in section 2.3, and a frame affixed to the rotating shaft takes the place of the forearm and upper arm frames. In this way, errors due to skin movement (inconsistent rotation axes) have been eliminated. The potential errors are now isolated to inaccuracy of IMU's calibration, parameter drift, and errors of the algorithm (for instance, integration error associated with the quaternion updating process). Note that since this rig has only one rotation axis, it cannot imitate the elbow FX/ES or any other multi segment movement, but it can be used to mimic the upper arm internal/external rotation, and the forearm pronation/supination.

During the test with the rotation rig, the handle was rotated manually clockwise and counterclockwise for two cycles, which mimicked the forearm PN/SN or upper arm IN/EX rotation. The angular displacement captured by the optical encoder was recorded at 50Hz and differentiated with respect to time to get the rotational velocity. An example comparison plot is shown in Figure 36, where the difference between the two systems is hardly visible. For statistical purpose, three different attitudes of the IMU on the holder were tested. For each attitude, 5 trials were obtained. Example results are shown in Figure 37. The blue solid lines

indicate the angular velocity recorded by encoder while the black solid line represents the difference between the IMU results and encoder results.

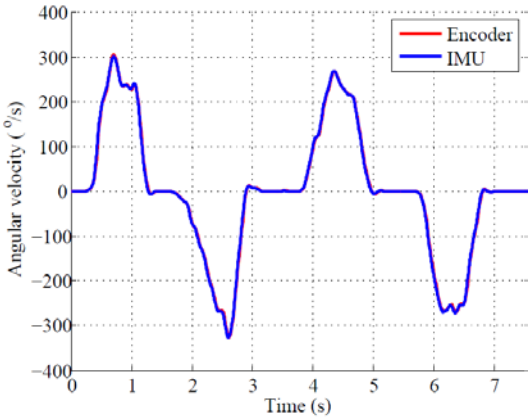

Figure 36 Comparison between IMU and single axis rotation rig

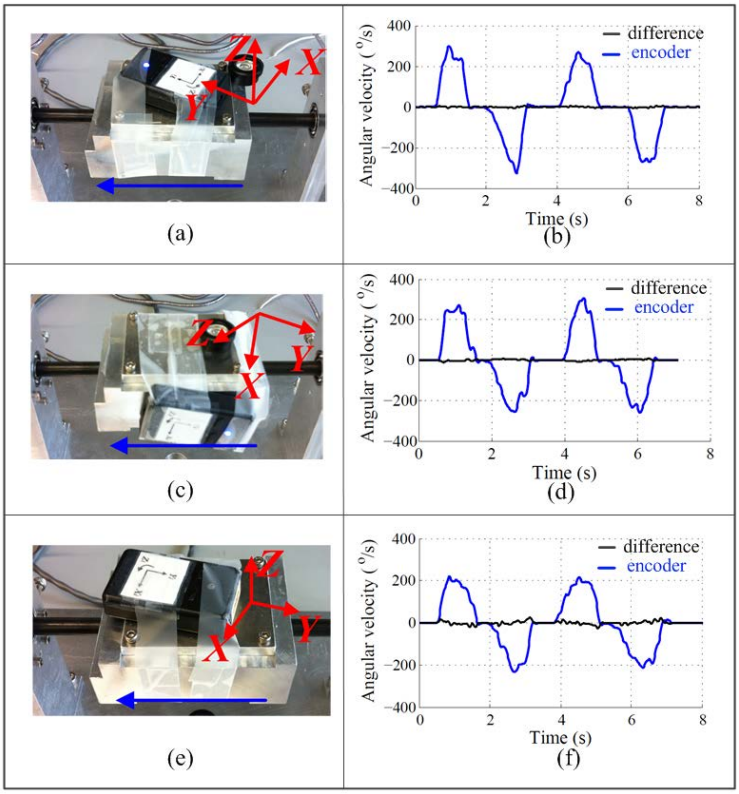

Figure 37 Comparison results on the single axis rotation rig.

The quantitative results are presented in Table 7. The mean values of the normalized RMSE between IMU system and rotation rig encoder data are less than 1%, while the peak value difference is from 0.7% to 1.89%, both of which are significantly improved compared to the validation results in the previous section. The mean value of zero-crossing timing difference is less than 1 sample interval. The paired t-test indicates that at the significance level of 0.95, there is no difference in zero-crossing timing for the two systems. These results suggest that the IMU is capable of accurately capturing segment rotations, and that the differences observed between IMU and video motion capture results are not due to IMU calibration, parameter drift, or the algorithm developed in this paper.

Table 7 Validation results of the single axis rotation rig experiment.

	Attitude 1		Attitude 2		Attitude 3	
	μ	σ	μ	σ	μ	σ
Normalized RMSE	0.6 (%)	0.2(%)	0.8(%)	0.2(%)	0.8(%)	0.1(%)
Peak value difference	0.7(%)	0.5(%)	1.7(%)	0.2(%)	1.9(%)	0.6(%)
Zero-crossing timing difference	-0.001(s)	0.008(s)	-0.002(s)	0.009(s)	-0.002(s)	0.008(s)

4.2.4 Kinematic chain timing of throwing motion

With the method and algorithm developed in this paper, the throwing motion can be decomposed into a combination of anatomical rotations, as shown in Figure 39 using an example data set. The complete throwing motion ranges from t=0s to t=2s. The stage from t=0s to t=0.5s is the early cocking period and is not shown in Figure 39. According to the zero-crossing timing of these rotational velocities, different anatomical rotation stages can be identified. At time t=1.46s, the elbow starts to extend, which is also considered to be the start point of the acceleration period of the throwing motion in this paper. The elbow extension ends at t = 1.71s. At time t = 1.59s, the

upper arm internal rotation begins, and it ends at t = 1.78s. Forearm pronation occurs over the time period from t = 1.77s to t=1.84s, which is located at the late stage of the acceleration period. The timing bars aligned at the bottom of Figure 39 clearly demonstrate the sequence as anatomical rotations propagate to complete the acceleration period of the throwing motion. It is worth mentioning that before each accelerating rotation, there is a period of opposite direction of rotation (also observed in the plots). For example, before the elbow extension, there is an elbow flexion period, which occurs from t = 0.88s to t =1.46s, in order to accumulate potential energy to boost the acceleration. Roach et. al. (Roach, Venkadesan et al. 2013) have studied this potential energy accumulation phenomenon in throwing motions using a video camera motion capture system, as shown in Figure 38. However, in the acceleration phase, the motion sequence of shoulder internal rotation, shoulder flexion and elbow extension was not identified. As Figure 39 illustrates, the multi-IMU system, using the zero-crossing method of angular rates, enables a straight-forward way to detail the timing of these anatomical rotations and analyze the kinematic chain of throwing more accurately.

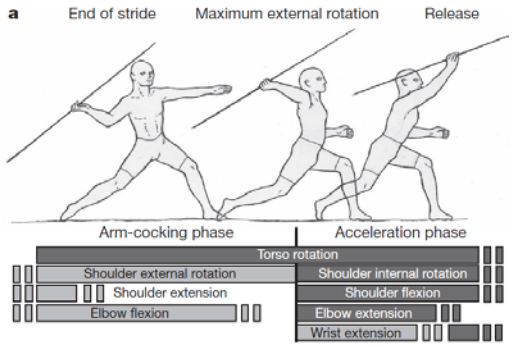

Figure 38 Decomposed rotations of a throwing motion

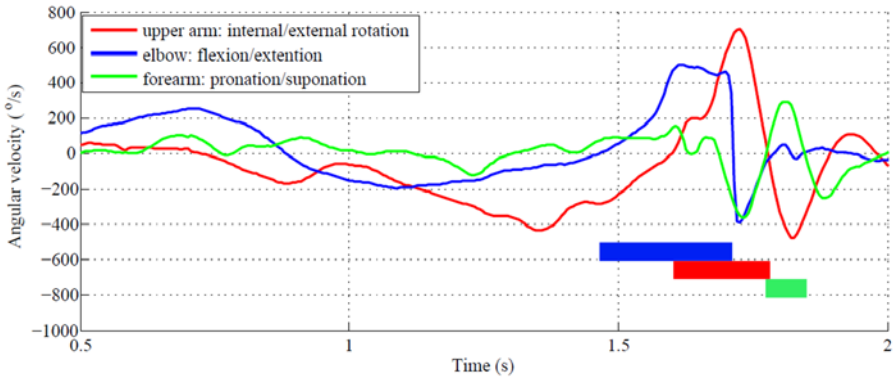

Figure 39 Anatomical rotation velocity and kinematic chain timing of throwing motion.

The kinematic chain timing plot, shown in Figure 39, can be projected onto the arm trajectory plot, as demonstrated in Figure 40, in order to accurately identify the critical events. For example, using this method, the arm position and attitude can be inspected at the start of acceleration stage. Then appropriate adjustments of arm posture can be made to improve performance. Note that this method removes all subjectivity of identifying phases of the arm motion that were highlighted in Fig. 26.

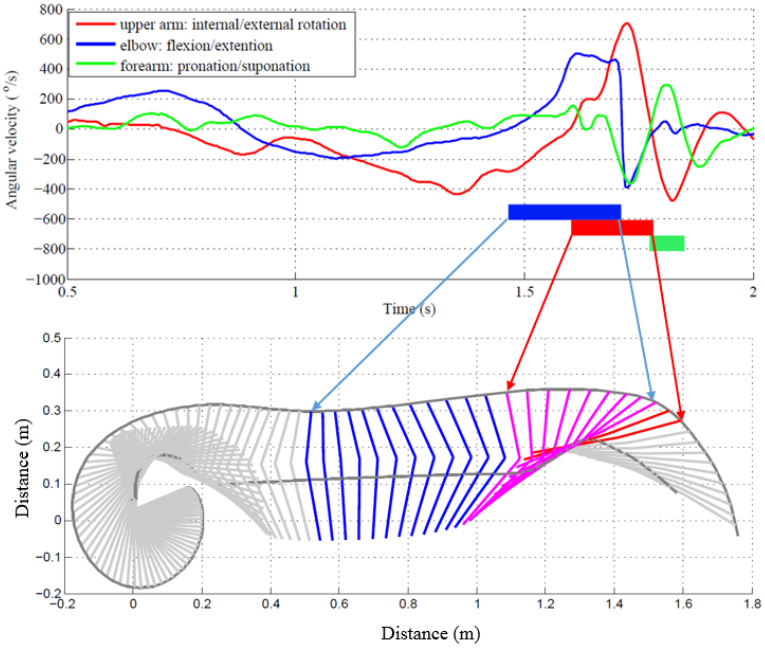

Figure 40 Kinematic chain timing represented on arm trajectory plot

4.3 CHAPTER SUMMARY

In this chapter, the throwing motion kinematics is reconstructed based on the method developed in Chapter 3. The trajectory of arm segments during throwing is calculated and validated by the video camera based motion capture system. The best case demonstrated the feasibility of the newly developed method. The error can be reduced when the hardware is improved on sampling frequency and data transmit reliability.

The arm anatomical rotations are the second part of kinematics reconstruction. There element rotations, forearm pronation/supination, elbow flexion/extension and upper arm internal/external rotation, are reconstructed. The experiment validation showed there was large amount of difference between the multi-IMU system and video camera system on anatomical rotation calculation. Then the validation on the single axis rotation rig has proven the multi-IMU system as well as the algorithm developed in this work is feasible and accurate in anatomical rotation calculation. The error was also partially due to the video camera system.

5.0 UPPER EXTREMITY KINETICS ANALYSIS FOR THROWING

In biomechanics studies, inverse dynamics analysis involves the calculation of kinetic quantities, for instance joint force and torque, from recorded kinematics data and a skeletal model (Riener and Straube 1997; Ren, Jones et al. 2008). Providing quantitative kinetic evidence, it is a useful tool for studying the mechanics of the throwing motion, as well as for monitoring and evaluating the risk level of injuries related to throwing (Hurd, Jazayeri et al. 2012; Oyama 2012). The conventional way to do inverse dynamics analysis is using camera based motion capture system to collect human motion data. In this study, a new approach is presented to carry out inverse dynamics analysis for throwing motions using multiple IMUs.

The overall framework of this multi-IMU based inverse dynamics analysis is shown in Figure 41. The raw data will go through coordinate frame transform operations in order to represent kinematics data in appropriate anatomical frames. Then these data will be input into an inverse dynamics model to calculate the kinetics, which includes total force and torque applied on the elbow and shoulder joints in this study.

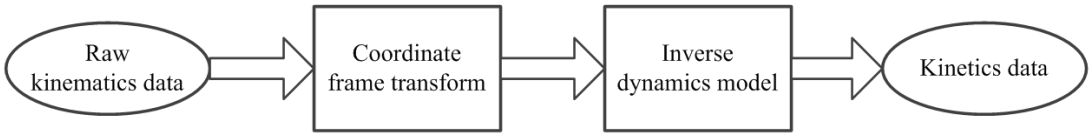

Figure 41 Overview of the IMU based inverse dynamics analysis

5.1 INVERSE DYNAMICS MODEL OF THROWING ARM

The inverse dynamics model uses kinematic quantities as inputs to calculate forces and torques applied on body segments. The arm model applied in this work is a double pendulum model, shown in Figure 42(a), which assumes that arm segments are rigid bodies. The elbow and shoulder are treated as ball and socket joints with 3-dimensional range of motion. The rigid body dynamics model of forearm and upper arm is demonstrated in Figure 42(b) and Figure 42(c) respectively (note that the hand is being lumped into the forearm in this model, as discussed in a later section). Although different groups of muscles and ligaments are used to generate forces and torques to drive the arm during throwing, the inverse dynamics method cannot identify kinetics for each muscle and ligament. Instead, this method can obtain lumped forces and torques applied on joints.

The IMU on the forearm is able to measure the linear acceleration of the spot to which the IMU is attached, as well as the angular velocity of forearm. Thus, according to rigid body kinematics theory (Greenwood 2006), linear acceleration of the forearm's center of mass can be obtained by Eq. (56):

$$a_{fmc} = a_{ifm} + \alpha_{ifm} \times L_{fmc/ifm} + \omega_{ifm} \times \left(\omega_{ifm} \times L_{fmc/ifm}\right) \quad \textbf{(56)}$$

where a_{ifm} is the linear acceleration of the IMU on the forearm, $L_{fmc/ifm}$ is the distance from IMU to forearm's center of mass. The parameters of Eq. (56) come with values represented in different frames, so coordinate frame transformations must be performed before calculating the result.

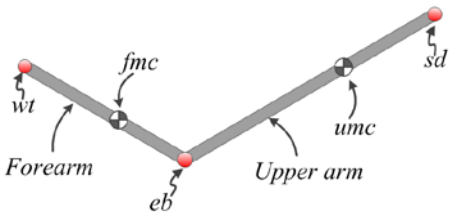

(a) Demonstration of the double pendulum model of arm

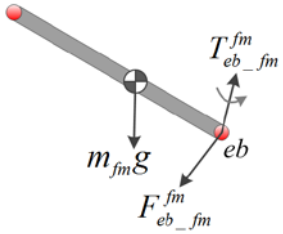

(b) Rigid body dynamics of forearm

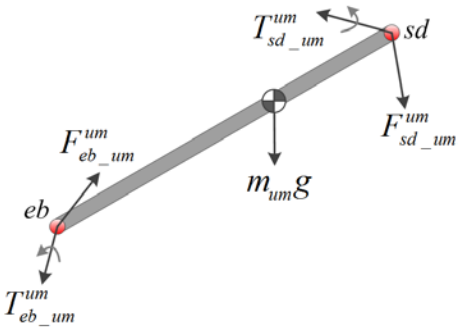

(c) Rigid body dynamics of upper arm

Figure 42 Rigid body dynamics model of 2-segmental arm

Besides, the reading of the accelerometer is the superposition of IMU's linear acceleration and gravitational reaction acceleration expressed in IMU's frame. The linear acceleration of this IMU in the forearm frame is obtained by:

$$a^{fm}_{ifm} = R^{fm}_{ifm} \cdot \left(a^{ifm}_{ifm} - R^{ifm}_{g} \cdot GR^{g}\right) \quad (57)$$

where a^{ifm}_{ifm} is the accelerometer's reading expressed in its own frame, $\boldsymbol{GR}^{g} = [0 \quad 0 \quad 9.81]^{T}$ is the gravitational reaction acceleration imposed on the accelerometer, and expressed in the global frame with unit m^2/s. R^{ifm}_{g} will transform the gravitational reaction acceleration into the IMU

frame, within which acceleration vector subtraction can be performed to remove the effect of the gravitational reaction force on the accelerometer. With Eq. (56), Eq. (57) can be rewritten to get the center of mass acceleration expressed in the anatomical frame, i.e. $\boldsymbol{F}^{fm}$:

$$a_{fmc}^{fm} = R_{ifm}^{fm} \cdot \left(a_{ifm}^{ifm} - R_g^{ifm} \cdot GR^g\right) + \alpha_{ifm}^{fm} \times L_{fmc/ifm}^{fm} + \omega_{ifm}^{fm} \times \left(\omega_{ifm}^{fm} \times L_{fmc/ifm}^{fm}\right) \quad \textbf{(58)}$$

With the similar analysis procedures, elbow acceleration a_{eb}^{um} and acceleration of upper arm center of mass a_{umc}^{um} can be calculated as shown in Eqs. (59) and (60) respectively:

$$a_{eb}^{um} = R_{ium}^{um} \cdot \left(a_{ium}^{ium} - R_g^{ium} \cdot GR^g\right) + \alpha_{ium}^{um} \times L_{eb/ium}^{um} + \omega_{ium}^{um} \times \left(\omega_{ium}^{um} \times L_{eb/ium}^{um}\right) \quad \textbf{(59)}$$

$$a_{umc}^{um} = R_{ium}^{um} \cdot \left(a_{ium}^{ium} - R_g^{ium} \cdot GR^g\right) + \alpha_{ium}^{um} \times L_{umc/ium}^{um} + \omega_{ium}^{um} \times \left(\omega_{ium}^{um} \times L_{umc/ium}^{um}\right) \quad \textbf{(60)}$$

where α_{ium}^{um}, ω_{ium}^{um}, α_{ifm}^{fm}, ω_{ifm}^{fm} are obtained by Eqs. (61) to (64) which transform the IMU's raw data into corresponding anatomical coordinate frames:

$$\alpha_{ium}^{um} = R_{ium}^{um} \cdot \alpha_{ium}^{ium} \quad \textbf{(61)}$$

$$\omega_{ium}^{um} = R_{ium}^{um} \cdot \omega_{ium}^{ium} \quad \textbf{(62)}$$

$$\alpha_{ifm}^{fm} = R_{ifm}^{fm} \cdot \alpha_{ifm}^{ifm} \quad \textbf{(63)}$$

$$\omega_{ifm}^{fm} = R_{ifm}^{fm} \cdot \omega_{ifm}^{ifm} \quad \textbf{(64)}$$

where ω_{i*m}^{i*m} is angular rate measured by gyroscopes, while α_{i*m}^{i*m} is angular acceleration which is obtained by one time differentiation of ω_{i*m}^{i*m}.

The anatomical lengths are measured after the sensors have been set up on the subject's arm. For instance, $L_{umc/ium}^{um}$ is the distance from the upper arm center of mass to the IMU on the upper arm, and measured from geometrical center of IMU to the average landmark dimension of upper arm center of mass reported by Dempster et. al. (Dempster and Gaughran 1967). Rotation matrices applied in this section are obtained by the method introduced in the previous section.

With the availability of kinematics data, the equations of motion can calculate the lumped force and torque applied on the elbow as shown by Eqs. (65) and (66):

$$F_{eb\_fm}^{fm} = m_{fm} \cdot \left(a_{fmc}^{fm} - R_g^{fm} \cdot G^g\right) \quad \textbf{(65)}$$

$$T_{eb\_fm}^{fm} = I_{fm/eb}^{fm} \cdot \alpha_{ifm}^{fm} + \omega_{ifm}^{fm} \times \left(I_{fm/eb}^{fm} \cdot \omega_{ifm}^{fm}\right) - L_{fmc/eb}^{fm} \times \left(m_{fm} \cdot R_g^{fm} \cdot G^g\right) \quad \textbf{(66)}$$

where $I_{fm/eb}^{fm}$ is forearm's moment of inertia matrix about the elbow joint, and the superscript *fm* indicates this vector is represented in forearm frame. m_{fm} is the mass of the forearm. $G^g = [0 \quad 0 \quad -9.81]^T$ is the gravitational acceleration expressed in the global frame.

For the same reason, the forces and torques associated with the upper arm muscles and ligaments are lumped to the shoulder. The corresponding equations of motion are:

$$F_{sd\_um}^{um} = m_{um} \cdot \left(a_{umc}^{um} - R_g^{um} \cdot G^g\right) - F_{eb\_um}^{um} \quad \textbf{(67)}$$

$$T_{sd\_um}^{um} = I_{um/sd}^{um} \cdot a_{ium}^{um} + \omega_{ium}^{um} \times \left(I_{um/sd}^{um} \cdot \omega_{ium}^{um}\right) - T_{eb\_um}^{um} - L_{eb/sd}^{um} \times F_{eb\_um}^{um} - L_{umc/sd}^{um} \times \left(m_{um} \cdot R_g^{um} \cdot G^g\right) \quad \textbf{(68)}$$

where $I_{um/sd}^{um}$ is upper arm's moment of inertia matrix about shoulder joint, $F_{eb\_um}^{um}$ and $T_{eb\_um}^{um}$ are elbow joint force and torque respectively applied on the upper arm, and demonstrated in Eqs. (69) and (70):

$$F_{eb\_um}^{um} = R_{fm}^{um} \cdot (-F_{eb\_fm}^{fm}) \quad \textbf{(69)}$$

$$T_{eb\_um}^{um} = R_{fm}^{um} \cdot (-T_{eb\_fm}^{fm}) \quad \textbf{(70)}$$

5.2 EXPERIMENT DEMONSTRATION AND RESULTS

The experiment validation setup, protocol and procedure are the same as those in the previous chapter. In order to validate the functionality and feasibility of the inverse dynamics analysis method in this work, only one subject's data is used. The subject was asked to throw a foam ball at a low level of exertion in order to avoid sensor saturation. The kinematics data was recorded by the IMUs during throwing.

The statistical properties of body segments, including weight and center of mass, are listed in Table 8 (Dempster and Gaughran 1967). These statistical values are used in this work. Because the hand is lumped to forearm in this model, the ratio of segment mass to the total body mass is adjusted to 2.1%, while the distance from proximal end to center of mass is adjusted to 57.3% of forearm length. Considering both forearm and upper arm to be ideal cylinders, the inertial properties were calculated and listed in Table 9.

Table 8 Properties of body segments

	Upper arm	Forearm & hand
Distance from proximal end to center of mass (%)	43.7	57.3
Ratio of segment mass to the total mass (%)	2.6	2.1

Table 9 Parameters of body segments of subject

Total mass (kg)	55
Upper arm length (m)	0.20
Forearm length (m)	0.22
Moment of inertia of forearm ($kg \cdot m^2$)	diag (0.0188, 0.0188, 0.0005)
Moment of inertia of upper arm ($kg \cdot m^2$)	diag (0.0194, 0.0194, 0.0012)

Applying these parameters and kinematic data as inputs to the inverse dynamics model, i.e. Eqs. (56) to (68), kinetics data can be generated. A sample test result on the human subject is shown in Figure 43.

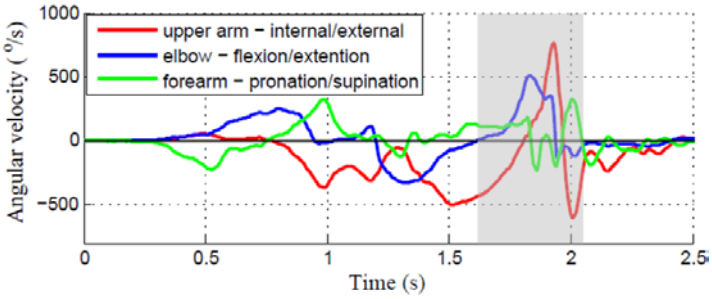

(a) Decomposed anatomical arm rotations

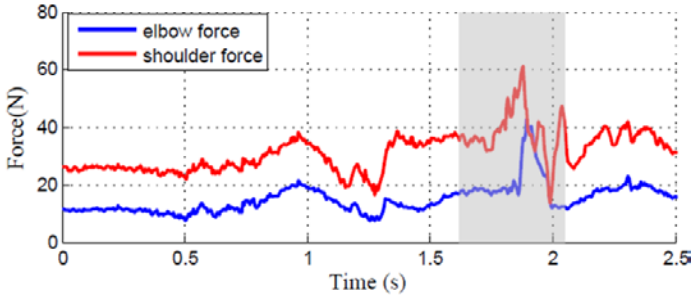

(b) Magnitude of total force on elbow and shoulder

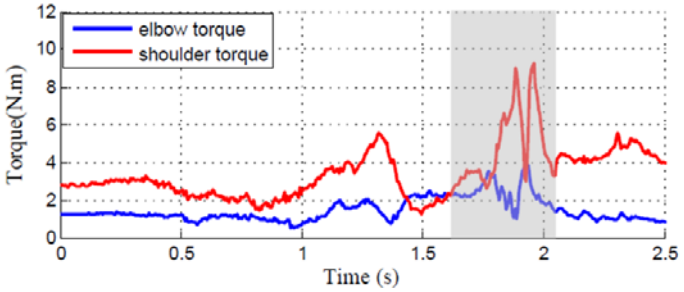

(c) Magnitude of total torque on elbow and shoulder

Figure 43 Inverse dynamics results of throwing motion

Figure 43(a) breaks down the arm motion into anatomical rotations, i.e. upper arm internal/external rotation, elbow flexion/extension and forearm pronation/supination. The acceleration stage of this sample throw starts at 1.61s when the elbow starts to extend, and

continues to 2.04s when the forearm pronation ends. This stage is highlighted by the grey areas on the three plots. Figure 43(b) and (c) demonstrates the magnitude of total force and torque applied on joints respectively during the throwing motion. From these plots, key events can be identified, such as peak torque and peak force of joints, as well as how they relate to anatomical rotations. Based on this information, it may be possible to evaluate the injury risk for each joint.

Projecting the peak joint force onto the arm trajectory plot, as shown in Figure 44, is an intuitive way to identify the riskiest moment during throwing and to inspect the movement mechanics.

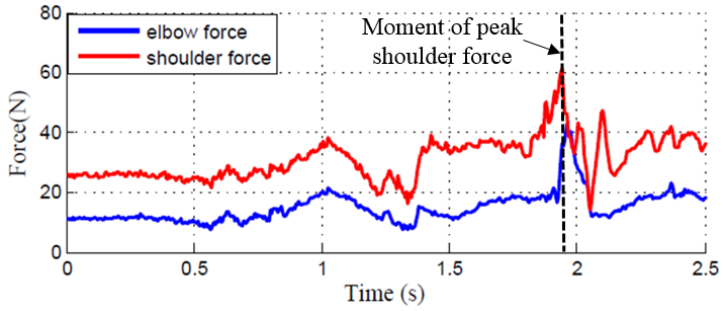

(a) Peak shoulder force moment

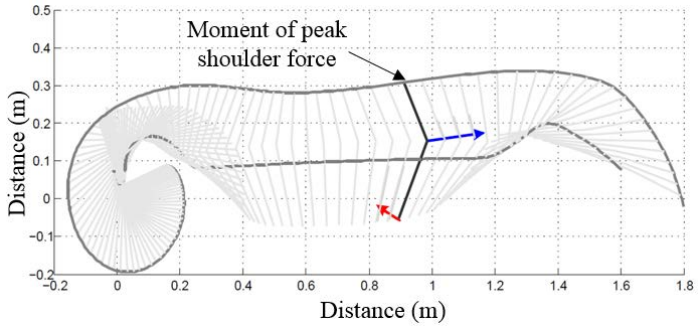

(b) Joint force demonstrated on arm trajectory plot

Figure 44 Projection of peak shoulder force moment onto arm trajectory plot

Another possible application of the inverse dynamics analysis is decomposing the total force and joint torque into pre-defined anatomical axes. As shown in Figure 45(a), the total torque on

the shoulder has been decomposed into radial and longitudinal direction. Because the moment of inertia about the longitudinal direction is relatively much smaller than that of the radial directions, the longitudinal component dominates the torque on the shoulder as shown in Figure 45(b). This decomposition can be carried out on any pre-defined anatomical coordinate axes in order to deliver useful information for injury analysis.

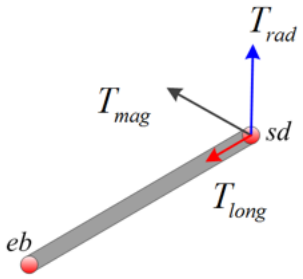

(a) Decomposition of the shoulder torque

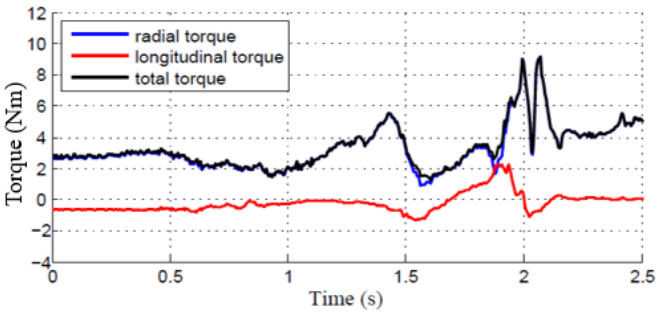

(b) Magnitude of radial and longitudinal torque on shoulder

Figure 45 Decomposition of the shoulder torque into radial and longitudinal directions

5.3 CHAPTER SUMMARY

This chapter has presented a new approach to carry out inverse dynamics analysis of throwing motions using the multi-IMU system designed in the previous chapters. A rigid body skeletal model of the throwing arm is built to calculate the kinetics quantities associated with elbow and

shoulder. A human subject experiment was presented to illustrate the method's use in measuring the kinetics of the throwing motion. The accuracy of this method will be validated in the future as it requires comparison to known standard force/torque measurement in a multiple body system. This method will enable monitoring of throwing kinetics with wearable IMUs, and may open the door to quantitative kinetics monitoring and injury risk evaluation.

6.0 DIGITAL FILTER DESIGN FOR SPORTS MOTION SIGNAL

Depending on the sensor signal types, numerical differentiation on raw data will be unavoidable in human motion signal processing. For example, in order to obtain angular acceleration of body segments for inverse dynamics calculations, a single differentiation at each time point must be applied on the gyroscope's output. This operation will introduce large errors because noise contained in raw data will be magnified by differentiation. The often-used solution is to design a low-pass filter to suppress noise before numerical differentiations. However, studies in recent years have reported that this method will also distort high frequency components in motion signals, which becomes more problematic as motion's speeds increase. Sometimes, those high frequency contents contain important information in specific human motion, for instance the impact force applied on the knee joint when jumping (Bisseling and Hof 2006; Kristianslund, Krosshaug et al. 2012). The throwing motion under study in this work is also such a case because high frequency signals dominate the acceleration stage of the throwing motion. In this chapter, the signal property will be investigated and a new digital filter will be designed to remove noise while keeping high frequency content during the dynamic period.

6.1 DRAWBACK OF THE CONVENTIONAL LOW-PASS FILTER

In order to investigate the effect of digital filters on sports motion signals, a baseline angular velocity signal of throwing motion was created. In the first place, a single axis gyroscope's digital reading was taken from a sample throwing motion. To remove the influence of unknown noise, a 3rd order Butterworth filter with normalized cutoff frequency of 0.3 was applied to get a smooth baseline angular velocity signal as shown in Figure 46(a). From the beginning to the sample point 900 is a quiet period, while sample points 900 to 1400 is a dynamic period, which is followed by another quiet period again to the end. A single numerical differentiation was applied on this angular velocity signal to obtain the baseline angular acceleration as shown in Figure 46(b). Note the increase in noisiness of the differentiated signal, although the numerical acceleration signal is still close to zero during the quiet periods.

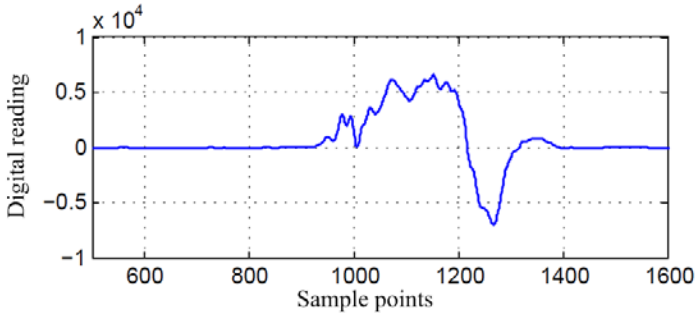

(a) baseline angular velocity signal

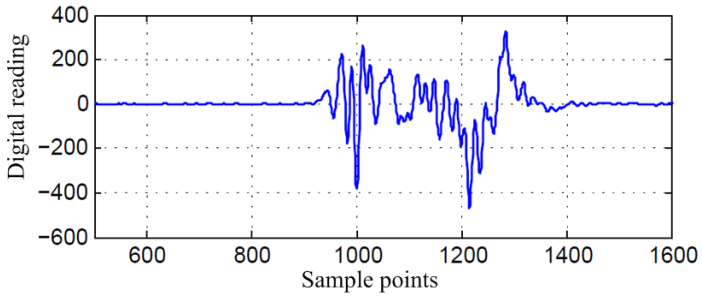

(b) baseline angular acceleration signal

Figure 46 Baseline signal of angular velocity and angular acceleration

Noises with different characteristics can be superposed on the baseline signal to study the effect of the digital filter. A white noise signal with magnitude 50 was superposed on the baseline angular velocity signal to represent the noisy signal and to demonstrate the feasibility of a new digital filter design for use in dynamic sports motion data.

Unsurprisingly, numerical differentiations will magnify noises significantly. As shown in Figure 47, only a single differentiation was performed on the noisy angular velocity to obtain the angular acceleration signal (red), which is compared to the baseline numerical angular acceleration (blue). The noise was magnified throughout the whole time history of the signal. For a camera-based motion capture system, this problem would be even worse since two numerical differentiation steps must be applied on marker position data to calculate both linear and angular accelerations.

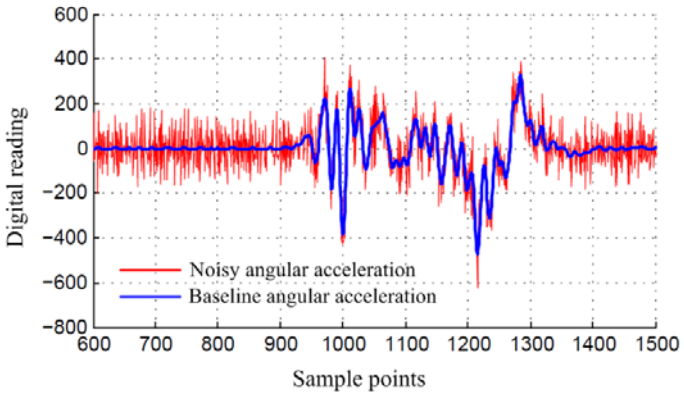

Figure 47 Effect of numerical differentiation on noise

The conventional method to deal with noise in motion capture system signals, both of IMU and video camera based system, is to apply a low-pass filter on the raw data before any numerical differentiations. To reproduce the drawbacks of this method, a low-pass filter (3rd order Butterworth filter with normalized cutoff frequency = 0.1) was applied on the noisy angular velocity signal to remove noise, and then a single differentiation was applied to get the

numerical angular acceleration signal. Figure 48 demonstrates the comparison between the filtered angular acceleration and its baseline signal. The noise at the still period was effectively removed by the low-pass filter. However, because the high frequency components dominate the dynamic period (roughly from sample points 900 to 1400) of throwing motion, this low-pass filter distorted the real signal content, especially those spikes which may contain important information on performance. In order to overcome the drawbacks of conventional low-pass filters, i.e. removing noise effectively without large distortion of the dynamic period signal, a switchable cut-off frequency low-pass filter will be developed in the next section.

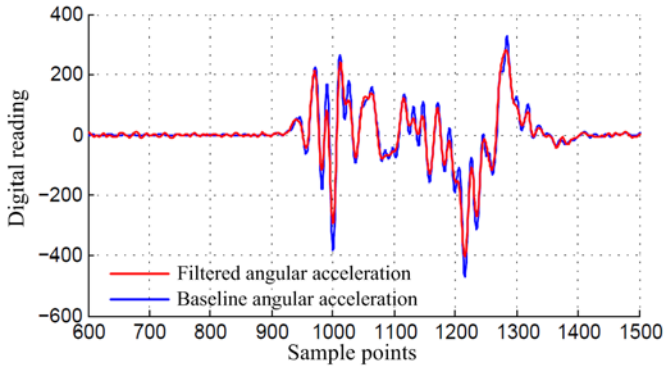

Figure 48 Comparison of LP filtered angular acceleration and baseline signal

6.2 FILTER DESIGN

Throwing motion consists of a quiet period and a dynamic period. The dynamic period includes acceleration and follow through stages which have relative higher signal magnitude and faster change rate compared to the quiet period which mainly contains cocking stage. An ideal filter, intuitively, should have switchable cut-off frequency which is able to remove high frequency noise during the quiet period while keep the high frequency signal components during the dynamic period. The wavelet transform is able to provide time information of discontinuities in a

signal. It is applied in this work to detect stage change time between quiet and dynamic periods. The structure of the filter designed in this work is shown in Figure 49. The raw motion data will go through a wavelet transform to get the stage change time information, which will decide the moment that the cut-off frequency needs to be switched. Then the raw motion data will be passed through this low-pass filter using different cut-off frequencies. It is worth noting that only two different cut-off frequencies are included in the switchable low-pass filter in this work because two different stages, quiet and dynamic, are defined in throwing motion signal. If more stages can be recognized during throwing, more cut-off frequencies can be included to treat different stages of the signal.

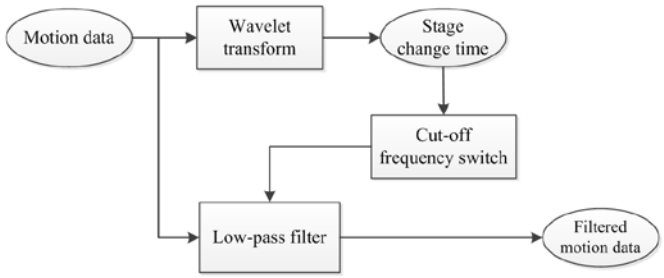

Figure 49 Structure of adaptive filter

After error and trial, a one-layer wavelet transform is applied in this work, whose structure is shown in Figure 50(a). A one-layer transform will decompose the raw signal (S) into level-1 approximation (A1) and level-1 detail (D1). The wavelet function applied is ‘db1’ as shown in Figure 50(b). The wavelet toolbox in Matlab was used to demonstrate the prototype of this digital filter.

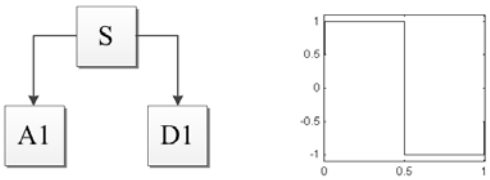

(a) one layer wavelet transform (b) db1 wavelet function

Figure 50 Wavelet transform structure and wavelet function

After applying the one-layer wavelet transform on the noisy angular velocity signal S, A1 and D1 components are shown in Figure 51. D1 contains the high frequency component of the signal S. During the still period, most of the high frequency components are white noise. During the dynamic period, high frequency components on the D1 plot include both white noise and the high frequency motion signal. Thus, the stage change can be recognized on the D1 plot. Namely, a threshold of D1 amplitude is used to recognize a stage change.

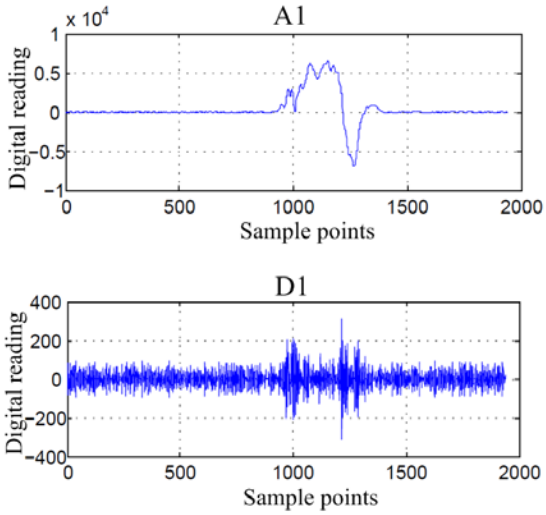

Figure 51 Wavelet transform of motion signal. A1: level 1 approximation; D1: level 1 detail.

After error and trial, a threshold of ±100 is applied on D1 to detect stage change time as t1 and t2, as shown in Figure 52. Therefore the dynamic period was determined to be from moment t1 to t2.

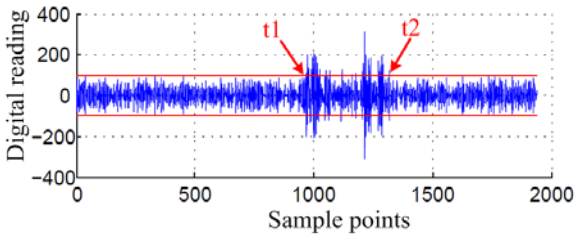

Figure 52 Stage change time captured by threshold =±100

The switchable cut-off frequency low-pass filter (SLP) was based on a 3rd-order Butterworth filter whose general form is shown in Eq. (71):

$$H(z) = \frac{b(0) + b(1)z^{-1} + b(2)z^{-2} + b(3)z^{-3}}{a(0) + a(1)z^{-1} + a(2)z^{-2} + a(3)z^{-3}} \quad (71)$$

In this work, only two different stages were recognized by the wavelet transform, thus two normalized cut-off frequencies were predefined: $\omega_n = 0.1$ for the quiet period and $\omega_n = 0.3$ for the dynamic period. Their corresponding parameter values are listed in Table 10.

After applying the SLP on the noisy angular velocity signal, a single differentiation was applied on the filtered signal to get the angular acceleration signal, which is compared to its baseline signal in Figure 53 (note that the blue line in Fig. 44 is the same as that in Fig. 37(b)).

Table 10 Value of digital filter parameters

ω_n	$a(0), a(1), a(2), a(3)$	$b(0), b(1), b(2), b(3)$
0.1	1, -2.3741, 1.9294, -0.5321	0.0029, 0.0087, 0.0087, 0.0029
0.3	1, -1.1619, 0.6959, -0.1378	0.0495, 0.1486, 0.1486, 0.0495

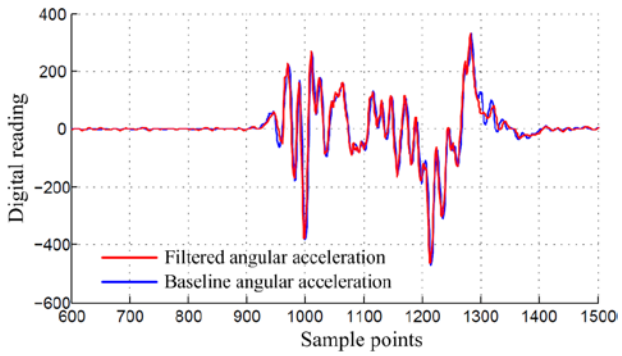

Figure 53 Comparison of SLP filtered angular acceleration and baseline signal

The comparison of Figure 47, Figure 48 and Figure 53 can draw the qualitative conclusion that the SLP filter is able to remove noise effectively during quiet periods and avoid signal distortion during the dynamic periods. The quantitative analysis is as follows: Table 11 lists the RMSE of processed angular acceleration data compared to the baseline signal at different stages. Note that the numbers in this table are based on the digital readings so are in units of bits. A perfect filter would result in RMSE values of zero, indicating that the filter returns an exact replica of the original (noiseless) signal. It is obvious that the conventional low pass filter can remove the noise during quiet periods but still has large errors during dynamic periods. The SLP filter, on the other hand, is almost as effective in removing quite period noise, but has improved fidelity during the dynamic period.

Table 11 RMSE of processed signal compared to baseline signal at different stages:

NLP: no filter, LP: conventional low-pass filter, SLP: switchable cut-off frequency filter

	Quiet period	Dynamic period
NLP	41.29	42.45
LP	1.99	26.41
SLP	2.12	19.69

In order to compare the effect of different filters on the peak values, four spikes were picked as shown in Figure 54. The comparison was performed between the filtered and baseline signals. The relative error *e* is defined as

$$e = \frac{|p_f - p_b|}{p_b} \times 100\% \qquad (72)$$

where p_b is the peak value of baseline signal, p_f is peak value of a filtered signal. The results are listed in Table 12.

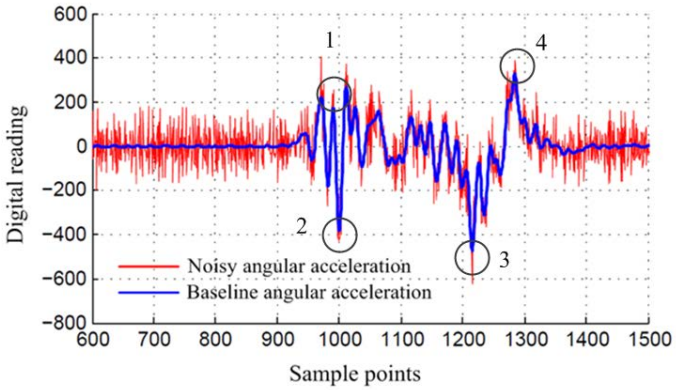

(a) error of NP on peak values

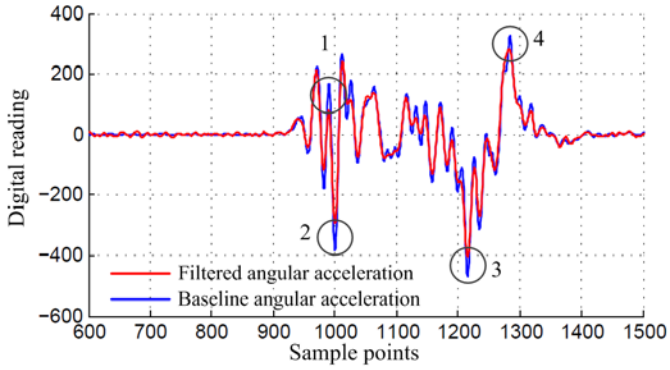

(b) error of LP on peak values

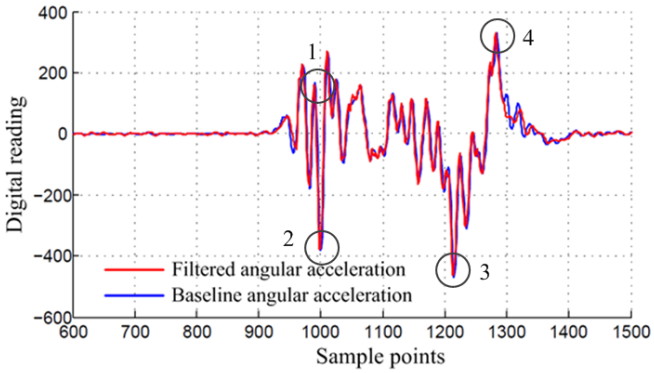

(c) error of SLP on peak values

Figure 54 Peak value data points for comparison between NP, SLP and LP processed data

Table 12 Peak value error comparison

	1	2	3	4
NLP	16.4%	13.0%	12.8%	20.6%
LP	54.7%	23.5%	14.7%	12.1%
SLP	3.5%	1.3%	0.4%	3%

From Table 12, the LP filter distorted the peak values up to 54.7%, which introduced a large error in angular acceleration calculation. The SLP filter designed in this work has an significant improvement to retain the accuracy of peak values.

6.3 CHAPTER SUMMARY

This chapter has addressed the common problem associated with filter design for human motion signals. A switchable cut-off frequency low-pass filter is designed. It contains a digital wavelet transform to detect stage change timing. Then a set of cut-off frequencies will be applied on different stages in order to remove the noise effectively throughout the signal while still keeping the high frequency content during the dynamic period. The quantitative comparison results have

demonstrated that the switchable cut-off frequency low-pass filter is able to lower the peak value error to 3.5% compared to 54.7% of conventional low-pass filter, while suppressing the high frequency noise at quiet period.

7.0 CONCLUSION

This dissertation has described a multi Inertial Measurement Unit based human sports motion analysis system. Towards the rotation matrix construction problem, the coordinate flow chart has been designed to visualize the coordinate frame transformation procedure and systematically construct 3-dimensional rotation matrices. With this newly designed analysis tool, a complete human motion kinematics and kinetics reconstruction algorithm have been developed thereafter, and applied to throwing motion with two inertial sensors.

In the kinematics study, the linear velocities and trajectories of arm segments were reconstructed. The experimental validation indicated that there was less than 7.2% difference on one axis between the IMU calculated trajectory and the video camera recorded marker trajectory. Considering there were sensor hardware limitations that affect the accuracy, the validation results were acceptable to prove the algorithm was feasible and accurate to reconstruct the arm segment trajectories. The second part of the kinematic study was calculation of anatomical rotations of the throwing arm, including forearm pronation/supination, elbow flexion/extension and upper arm internal/external rotation. The experimental validation indicated that results of the multi-IMU system and video camera system generally match each other very well. The normalized RMSE was 2.7±0.4 % at the best case. However, there was a large amount of difference on peak rotational velocities calculated by the two systems. In order to validate the peak rotational velocity calculation accuracy of the algorithm designed in this work, a single axis

rotation rig test was carried out to prove that the algorithm developed in this work was accurate. Test results using the rotation rig showed that the inertial measurement algorithm produced 1.9±0.6 % normalized RMSE even at the worst case. Zero crossing times were also validated to be accurate, which is essential in kinematic chain timing reconstruction.

The inverse dynamics study started with the establishment of a rigid body skeletal model of the throwing arm. The kinematics data was input into the model to generate lumped torque and force imposed on shoulder and elbow joints. The human subject experiment verified the functionality and feasibility of the inverse dynamics analysis procedure.

In the last part of this dissertation, a low-pass digital filter with switchable cut-off frequency was designed to improve the noise suppression of numerical differentiation on human sports motion signals. A discrete wavelet transform was used to detect the transition from quiet periods and dynamic periods during the throwing event. Two different low-pass filters with pre-defined cut-off frequencies were then applied on different stages of the motion signal in order to suppress noise during the quiet period without adding distortion during the dynamic period.

The motion analysis algorithm developed in this work is expandable to include any number of IMUs and can be applied to any type of sports motion. This dissertation has made contributions to human motion analysis in the following aspects:

1. Sports motion analysis algorithm
    a. Designed the coordinate flow chart method which enables a systematic way to construct rotation matrices, and an expandable framework for multi-IMU applications;

b. Developed a motion analysis algorithm which is able to calculate arm trajectories, anatomical rotations, and torques and forces on joints, for various kinematics and kinetics analyses of human motion.

2. Algorithm validation:
    a. Validated the accuracy of kinematics results by human subject experiments, and showed that the algorithm developed in this work is feasible for human sports motion reconstruction;
    b. Validated the accuracy of rotation reconstruction results on a single axis rotation rig, and proved that the multi-IMU system provides better accuracy on arm rotations calculation than the video camera system.
3. Sports mechanics study:
    a. Demonstrated kinematic chain timing construction by multi-IMU system, and showed more details on rotation sequence than previous work;
    b. Demonstrated kinetic analysis applications using multi-IMU system, including locating instant of highest joint load during throwing.
4. Digital filter design:
    a. Designed a digital low-pass filter which is able to suppress noise during quiet periods while still keep high frequency components of signal during dynamic periods.

Sensor hardware limitation is the biggest challenge for wide application of this algorithm and motion analysis system. With the increasing sensor measurement range, this motion analysis algorithm will play a more and more important role in sports related training, coaching, rehabilitation and scientific research in near future.

APPENDIX

CALIBRATION OF INERTIAL MEASUREMENT UNIT

Most commercially available IMUs have been calibrated by vendors before delivery to customers. However, due to the inherent parameters that cause drifting of the MEMS motion sensors, re-calibrations must be carried out by users before using the IMUs. The measurement parameters of the sensors, especially the bias of the MEMS rate gyroscopes is affected by environment temperature and moisture (Choa 2005; El-Diasty, El-Rabbany et al. 2007), and random drifting. This parameter drifting will cause an unbounded error accumulation in calculating kinematic quantities which involves numerical integrations.

The IMU calibration procedure involves comparing known physical quantities to sensor outputs to determine the measurement parameters, such as sensitivity, bias and other factors. An ideal calibration, which requires creating an accurate known physical quantity, usually means expensive instruments, for instance, a turntable generating constant accurate angular velocity. In addition, due to the fact mentioned above that these parameters are changing over time, frequent calibrations are needed to maintain accurate measurements. For these reasons, a simple and low cost method to calibrate the IMU is necessary no matter for the purpose of lab use or commercial applications.

Different methods for calibrating inertial sensors and magnetometers are proposed in the literature. The underlying common point is making use of naturally existing physical quantities to calibrate sensors. For example, when the IMU is held stationary, the accelerometer is measuring gravity while the magnetometer is measuring the environmental magnetic field. As for the gyroscope, the time integration of the gyroscope output during a pre-defined rotation will be compared to the known angle it has rotated (Jurman, Jankovec et al. 2007; Fong, Ong et al. 2008).

Calibration methods can be classified into three categories: Min-Max(Aggarwal, Syed et al. 2008), ellipsoid fitting (Gietzelt, Wolf et al. ; Skog and Händel 2006; Jurman, Jankovec et al. 2007; Fong, Ong et al. 2008; Bonnet, Bassompierre et al. 2009; Vasconcelos, Elkaim et al. 2011), and filter design. Combinations of these methods are also employed. The fundamental principle of the Min-Max method is alignment of the sensor's sensitive axis parallel and antiparallel to the direction of the reference physical quantity. Then, the bias and sensitivity can be calculated by the minimum and maximum sensor output of each axis. For sake of its ease for use, the Min-Max approach will be applied in this work for accelerometer calibration. Because the rotation motion will not affect the magnetic field measurement, and since the environmental magnetism direction is unknown, the ellipsoid fitting method is suitable for magnetometer calibration. Since accurate angle measurement is easier to obtain than angular velocity, the gyroscope output will be integrated with respect to time to compare with a known angle increment. The following sections will explain the details of these calibration procedures.

A.1 INERTIAL SENSOR AND MEASUREMENT MODEL

The vendor's specification for IMUs is listed in Table 13 (Yost Engineering 2013). The highest available measurement range of this IMU, ±2,000 (°/sec) for the gyroscope and ±24 (g) for the accelerometer, is selected because sports motion in this study is high speed and short duration. Although the sensitivity has to be sacrificed to utilize the highest measurement range, it will not be a critical problem in short time motion measurements, whereas saturation would be a more serious problem in this study.

Table 13 Manufacturer specification of the IMU

Sensor type	Range	Sensitivity
Accelerometer	±24(g)	0.012 (g/digit)
Gyroscope	±2,000 (°/sec)	0.07 (°/sec/digit)
Magnetometer	1.3 (Ga)	5 (mGa/digit)

The calibration procedure involves determining the parameter values in a generic measurement model for a tri-axial sensor, shown in Eq. (73). The measurement model describes the relationship between physical quantity $\vec{p} = (p_x \quad p_y \quad p_z)^T$ and its corresponding sensor digit reading $\vec{r} = (r_x \quad r_y \quad r_z)^T$, and is feasible for any tri-axial sensor.

$$\begin{bmatrix} p_x \\ p_y \\ p_z \end{bmatrix} = \begin{bmatrix} s_x & c_{12} & c_{13} \\ c_{21} & s_y & c_{23} \\ c_{31} & c_{32} & s_z \end{bmatrix} \cdot \left\{ \begin{bmatrix} r_x \\ r_y \\ r_z \end{bmatrix} - \begin{bmatrix} b_x \\ b_y \\ b_z \end{bmatrix} - \begin{bmatrix} \varepsilon_x \\ \varepsilon_y \\ \varepsilon_z \end{bmatrix} \right\} \qquad \textbf{(73)}$$

In matrix *C* (3×3), the diagonal elements $(s_x \quad s_y \quad s_z)$ are sensitivity, while the off-diagonal elements $(c_{12} \quad c_{13} \quad c_{21} \quad c_{23} \quad c_{31} \quad c_{32})$ combine the minor effect of misalignment, non-orthogonality, cross sensitivity and etc.. The vectors $\vec{B} = (b_x \quad b_y \quad b_z)^T$ and $\vec{\varepsilon} = (\varepsilon_x \quad \varepsilon_y \quad \varepsilon_z)^T$ represent the bias and noise respectively. The motion under study is short duration, typically less than five seconds, and will not be affected significantly by those minor

factors. For the sake of simplifying the calibration procedure, only sensitivity (diagonal elements of matrix C) and bias ($\vec{B}$) of the measurement model will be determined by the following procedures.

A.2 SENSOR CALIBRATION PROCEDURE AND RESULTS

A.2.1 Calibration of gyroscope

As mentioned in previous section, a turntable providing accurate rotation rate usually means an expensive investment. In this work, a low cost calibration rig is designed as shown in Figure 55. The motor will drive the IMU holder to rotate while the encoder will record the angle increment.

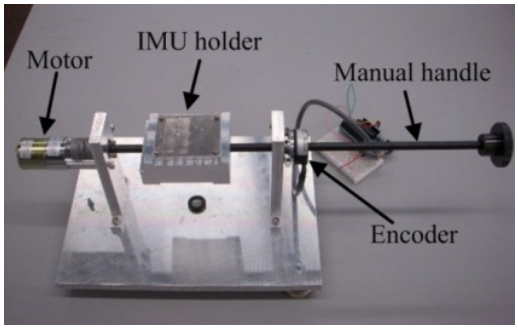

Figure 55 IMU calibration rig

The calibration procedures have been designed as follows:

Step 1. Fix the IMU on the IMU holder with one sensitive axis aligned with the rotation axis. Keep the IMU in stationary status for around 10 seconds. This period is denoted as STA_i, (i=x,y,z) in later analysis;

Step 2. Rotate the IMU at any speed for about 20 revolutions, and denote this period as ROT_i, (i=x,y,z);

Step 3. Align another sensitive axis to the rotation axis and repeat steps 1-2 until all of the three axes are calibrated.

Figure 56 shows gyroscope output for x axis calibration. Since the gyroscope bias is drifting all the time, the output at stationary period STA_x will be averaged to be the temporary bias to compensate data at the adjacent ROT_x indicated by Eq. (74). Worth noting is that the gyroscope bias needs to be recalibrated every time, even after calibration. This process will be explained later.

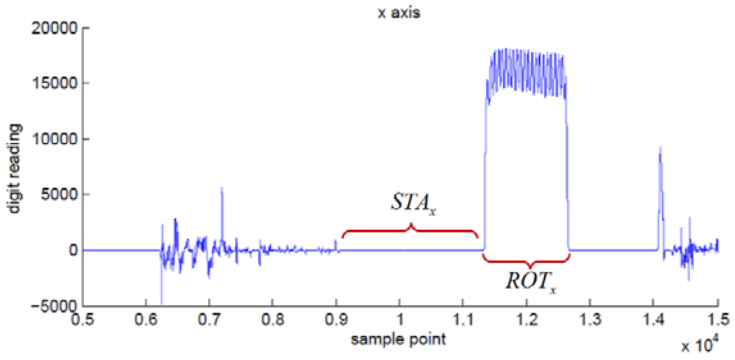

Figure 56 Gyroscope calibration output

The bias for that axis is then determined by:

$$b_{gx} = mean\big(output(STA_x)\big) \quad (74)$$

The time integration of the gyroscope output with bias compensation equals the angle increment recorded by the encoder. Thus the sensitivity of the axis is obtained by:

$$S_{gx} = \frac{E_{ang}}{\sum_{ROT_x}(g_k - b_{gx}) \cdot \Delta T_x} \quad (75)$$

where ΔT_x is the sample interval, g_k is gyroscope output at instance k in the ROT_x time period, E_{ang} is the angle increment (measured by the encoder) during the ROT_x time period. The calibration procedure is repeated for the other two axes so that all of the gyroscope sensitivities are calibrated.

Gyroscope bias drifts much faster than the other sensor parameters in the IMU, thus it needs to be calibrated every time before use and even during the testing. This is done by considering the gyroscope output when it is in stationary status. For example, during testing the subject equipped with IMUs will be asked to stand still for 10 to 15 seconds which allows the gyroscope to record stationary output. Eq. (74) is then used to obtain the gyroscope bias for measurement.

A.2.2 Calibration of accelerometer

The reference physical quantity for accelerometer calibration is gravitational acceleration, whose direction is strictly upwards. (The gravitational reaction force is upwards when the IMU is stationary, leading to an upward sense in the MEMS accelerometer measurement). An aluminum block with squarely machined surfaces will aid in alignment of the IMU axes with the gravitational field as shown as in Figure 57. One of the IMU edges is aligned to be coincident with the block edge, which with the help of a bullseye level ensures the edge is aligned properly. Thereafter, rotating the aluminum block and IMU in sequence, the 6-orientation Min-Max calibration procedure is applied as follows:

Step 1: Align the IMU with the preset orientation in a sequence as shown in Figure 58;

Step 2: At each orientation, leave the IMU in stationary status for 10 seconds. Calculate the accelerometer parameters using Eqs. (74) and (75).

Figure 57 Accelerometer calibration: align one axis of IMU with gravitational reaction force

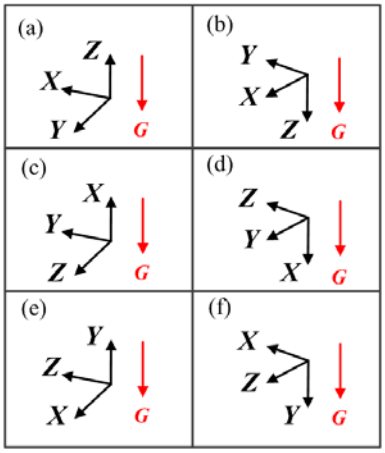

Figure 58 Six orientation sequence for accelerometer calibration

Eqs. (76) and (77) show example accelerometer parameter calculations for which the *x* axis is aligned with respect to +***G*** and –***G*** directions:

$$b_{ax} = \frac{A_x^{+g} + A_x^{-g}}{2} \qquad (76)$$

$$S_{ax} = \frac{2}{A_x^{+g} - A_x^{-g}} \qquad (77)$$

where A_x^{+g} and A_x^{-g} are mean values of the accelerometer *x* axis output while the IMU is aligned as in Figure 58 (c) and (d), respectively, during the calibration time period. The procedure is repeated for the other two axes to get the sensitivity and bias of all accelerometers.

A.2.3 Calibration of magnetometer

The indoor environmental magnetic field will be used for magnetometer calibration. However, the indoor magnetic field has complicated components including earth magnetism, metal material effects, and those generated by electronic devices. Thus, it is impossible to get a consistent magnetic field for calibration purpose. Since the current study uses the magnetometers to detect the heading angle of the IMUs deployed on human body segments, the absolute value of magnetic field strength is unnecessary. In this work, the calibration method assumes that within a small range of space which is away from (at least half a meter) any magnetic material and electronic devices the magnetic field is considered to be a stable, unity reference quantity with which to calibrate the magnetometer. Once calibrated, any two magnetometers are able to provide the relative heading angle as long as they are measuring the same magnetic field, no matter its true direction or value. To ensure the validity of this assumption, the two magnetometers should be always close during calibration and testing.

The calibration procedure involves rotating an IMU within a small space at arbitrary attitude. Example raw magnetometer data is shown in Fig. 10. The magnetometer will record the same magnetism vector at many different orientations. These measurements construct an ellipsoid rather than a sphere in magnetometer coordinates, as shown in Figure 60, due to undetermined value of measurement model parameters. An optimization method is applied thereafter which will correct the 3-dimensional plot of measurements into a unit radius sphere.

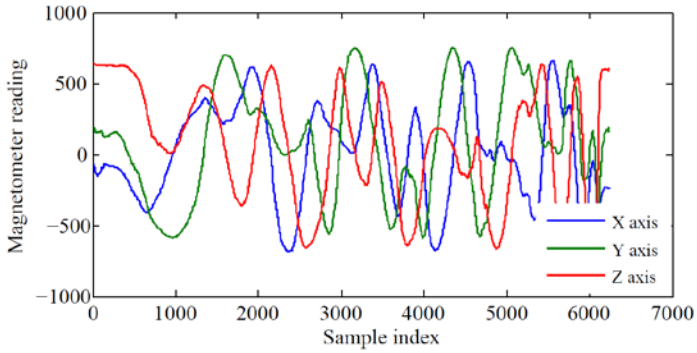

Figure 59 Raw data of magnetometer calibration

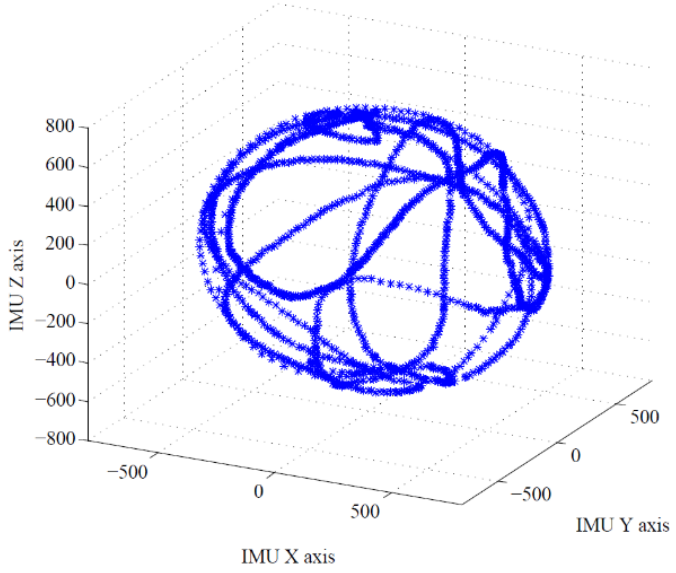

Figure 60 Three dimensional view of magnetometer measurement

The optimized parameters and objective function is set by Eqs. (78) and (79):

$$\hat{\theta} = \arg\min_{\theta}\{L(\theta)\} \tag{78}$$

$$L(\theta) = \sum_{i=1}^{n}\left(\left\|\vec{P}_i\right\|^2 - \left\|C \cdot \left(\vec{R}_i - \vec{B}\right)\right\|^2\right)^2 \tag{79}$$

where variable parameters set $\theta = (S_x \quad S_y \quad S_z \quad b_x \quad b_y \quad b_z)$ represents diagonal elements in matrix C and bias vector $\vec{B}$ of magnetometer's measurement model. Other off-diagonal elements and the noise vector are assumed to be zero. $\vec{P}_i$ is the magnetic vector measured by the sensors at

each moment. Since the environmental magnetic strength is assumed to be unity within the space for calibration, Eq. (80) is set up to supplement the objective function of Eq. (79):

$$\left\|\vec{P}_i\right\| = 1 \ (\forall \ i) \qquad \textbf{(80)}$$

An issue in calibrating magnetometers is that improper selection of the initial value for parameter set θ may cause divergence for the final estimation due to the reason that the sensors parameters have large variation. The initial guesses of the bias and sensitivity for axis *i* (*i* = *x*, *y*, *z*) are estimated in Eqs. (81) and (82), respectively:

$$b_{mi,0} = \frac{m_{i,max} + m_{i,min}}{2} \qquad \textbf{(81)}$$

$$S_{mi,0} = \frac{1}{m_{i,max} - b_{mi,0}} \qquad \textbf{(82)}$$

where $m_{i,max}$ and $m_{i,min}$ are maximum and minimum value of each axis *i* in Figure 59.

The procedure of calibrating magnetometers is summarized as follows:

Step 1: Hold the IMU in a space which is away (at least half meter) from magnetic material, metals and electronic devices;

Step 2: Rotate the IMU slowly at as many orientations as possible, meanwhile make sure the IMU is staying in the small range of space;

Step 3: Data preprocess: initial value calculation for parameters (Eq. (80) and (81)) and objective function setup (Eqs. (78) and (79));

Step 4: Parameter initial values and objective function will be input into the Matlab optimization toolbox, and *fminsearch* routine will be used to minimize the objective function to achieve the optimized estimation for the parameter set.

Summary

This chapter addressed the issue of calibrating sensors in the IMUs applied in this work. Based on the generic sensor measurement model, dominant parameters are taken into account for the sake of simplifying the calibration procedure. The calibration procedure is designed to determine the sensitivity and bias of accelerometers and magnetometers as well as the gyroscope sensitivity. Since the bias of gyroscope has much more serious drift compared to the other sensors, it should be calibrated in every test. The calibration results of the two IMUs used in this work are listed in Table 14:

Table 14 Calibration results

	Spec	IMU 1			IMU 2		
		X	Y	Z	X	Y	Z
Gyroscope sensitivity (°/sec/digit)	0.07	0.0725	0.07	0.0687	0.0683	0.0694	0.0698
Accelerometer sensitivity (g/digit)	0.012	7.52e-04	7.31e-04	7.34e-04	7.30e-04	7.36e-04	7.37e-04
Accelerometer bias (digit)	N/A	-83.42	14.231	-180.655	-203.567	122.915	-255.412
Magnetometer bias (digit)	N/A	-18.499	94.599	-15.113	-15.946	72.666	-20.865
Magnetometer sensitivity (1/digit)	N/A	0.0022	0.0023	0.0023	0.0022	0.0023	0.0024

BIBLIOGRAPHY

Acar, C. and A. M. Shkel (2003). "Experimental evaluation and comparative analysis of commercial variable-capacitance MEMS accelerometers." Journal of Micromechanics and Microengineering **13**(5): 634.

Aggarwal, P., Z. Syed, et al. (2008). "A standard testing and calibration procedure for low cost MEMS inertial sensors and units." Journal of navigation **61**(02): 323-336.

Aguinaldo, A., J. Buttermore, et al. (2003). "Sequential body motion and shoulder joint torque between baseball pitchers of various levels." J Appl Biomech.

Barris, S. and C. Button (2008). "A review of vision-based motion analysis in sport." Sports Medicine **38**(12): 1025-1043.

Bisseling, R. W. and A. L. Hof (2006). "Handling of impact forces in inverse dynamics." Journal of biomechanics **39**(13): 2438-2444.

Bonnet, S., C. Bassompierre, et al. (2009). "Calibration methods for inertial and magnetic sensors." Sensors and Actuators A: Physical **156**(2): 302-311.

Brennan, A., J. Zhang, et al. (2011). "Quantification of inertial sensor-based 3D joint angle measurement accuracy using an instrumented gimbal." Gait & posture **34**(3): 320-323.

Bushnell, B. D., A. W. Anz, et al. (2010). "Association of maximum pitch velocity and elbow injury in professional baseball pitchers." The American Journal of Sports Medicine **38**(4): 728-732.

Caruso, M. J., T. Bratland, et al. (1998). "A new perspective on magnetic field sensing." SENSORS-PETERBOROUGH- **15**: 34-47.

Chardonnens, J., J. Favre, et al. (2012). "A system to measure the kinematics during the entire ski jump sequence using inertial sensors." Journal of biomechanics.

Choa, S.-H. (2005). "Reliability of vacuum packaged MEMS gyroscopes." Microelectronics Reliability **45**(2): 361-369.

Chow, T. S. (1978). "Testing software design modeled by finite-state machines." Software Engineering, IEEE Transactions on(3): 178-187.

Cooper, G., I. Sheret, et al. (2009). "Inertial sensor-based knee flexion/extension angle estimation." Journal of biomechanics **42**(16): 2678-2685.

Craft, L. L., T. M. Magyar, et al. (2003). "The relationship between the Competitive State Anxiety Inventory-2 and sport performance: A meta-analysis." Journal of Sport and Exercise Psychology **25**(1): 44-65.

Cutti, A. G., A. Giovanardi, et al. (2008). "Ambulatory measurement of shoulder and elbow kinematics through inertial and magnetic sensors." Medical & biological engineering & computing **46**(2): 169-178.

CyberGlove "CyberGlove II."

De Vries, W., H. Veeger, et al. (2010). "Functionally interpretable local coordinate systems for the upper extremity using inertial & magnetic measurement systems." Journal of biomechanics **43**(10): 1983-1988.

Delp, S. L., F. C. Anderson, et al. (2007). "OpenSim: open-source software to create and analyze dynamic simulations of movement." Biomedical Engineering, IEEE Transactions on **54**(11): 1940-1950.

Dempster, W. T. and G. R. Gaughran (1967). "Properties of body segments based on size and weight." American Journal of Anatomy **120**(1): 33-54.

Devices, A. (2011). ADXRS649.

Diebel, J. (2006). "Representing attitude: Euler angles, unit quaternions, and rotation vectors." Matrix.

Ekstrand, J., M. Hägglund, et al. (2011). "Injury incidence and injury patterns in professional football: the UEFA injury study." British Journal of Sports Medicine **45**(7): 553-558.

El-Diasty, M., A. El-Rabbany, et al. (2007). "Temperature variation effects on stochastic characteristics for low-cost MEMS-based inertial sensor error." Measurement Science and Technology **18**(11): 3321.

El-Gohary, M. and J. McNames (2012). "Shoulder and Elbow Joint Angle Tracking With Inertial Sensors." Biomedical Engineering, IEEE Transactions on **59**(9): 2635-2641.

Emery, C. A., B. Hagel, et al. (2010). "Risk factors for injury and severe injury in youth ice hockey: a systematic review of the literature." Injury prevention **16**(2): 113-118.

Faber, G. S., I. Kingma, et al. (2010). "Bottom-up estimation of joint moments during manual lifting using orientation sensors instead of position sensors." Journal of biomechanics **43**(7): 1432-1436.

Favre, J., R. Aissaoui, et al. (2009). "Functional calibration procedure for 3D knee joint angle description using inertial sensors." Journal of biomechanics **42**(14): 2330.

Favre, J., B. Jolles, et al. (2008). "Ambulatory measurement of 3D knee joint angle." Journal of biomechanics **41**(5): 1029-1035.

Fleisig, G. S., J. R. Andrews, et al. (2011). "Risk of Serious Injury for Young Baseball Pitchers A 10-Year Prospective Study." The American Journal of Sports Medicine **39**(2): 253-257.

Fleisig, G. S., J. R. Andrews, et al. (1995). "Kinetics of baseball pitching with implications about injury mechanisms." The American Journal of Sports Medicine **23**(2): 233-239.

Fong, W., S. Ong, et al. (2008). "Methods for in-field user calibration of an inertial measurement unit without external equipment." Measurement Science and Technology **19**(8): 085202.

Freescale (2008). "MMA6280QT Dual axis low-g micromachined accelerometer."

Ghasemzadeh, H. and R. Jafari (2011). "Coordination Analysis of Human Movements With Body Sensor Networks: A Signal Processing Model to Evaluate Baseball Swings." Sensors Journal, IEEE **11**(3): 603-610.

Gietzelt, M., K.-H. Wolf, et al. "Performance comparison of accelerometer calibration algorithms based on 3D-ellipsoid fitting methods." Computer Methods and Programs in Biomedicine(0).

Greenwood, D. T. (2006). Advanced Dynamics, Cambridge University Press.

Hirashima, M., H. Kadota, et al. (2002). "Sequential muscle activity and its functional role in the upper extremity and trunk during overarm throwing." Journal of sports sciences **20**(4): 301-310.

Hirashima, M., K. Yamane, et al. (2008). "Kinetic chain of overarm throwing in terms of joint rotations revealed by induced acceleration analysis." Journal of biomechanics **41**(13): 2874-2883.

Honeywell. "3-Axis Digital Compass IC HMC5883L." from www.honeywell.com.

Hurd, W. J., R. Jazayeri, et al. (2012). "Pitch Velocity Is a Predictor of Medial Elbow Distraction Forces in the Uninjured High School–Aged Baseball Pitcher." Sports Health: A Multidisciplinary Approach **4**(5): 415-418.

Inc., T. M. (2012). Matlab. Natick, Massachusetts.

InvenSense, I. (2013). "Nine-Axis MEMS Motion Tracking Devices." from http://www.invensense.com/mems/gyro/nineaxis.html.

Ismail, A. R. and S. S. Asfour (1999). "Discrete wavelet transform: a tool in smoothing kinematic data." Journal of biomechanics **32**(3): 317-321.

Jurman, D., M. Jankovec, et al. (2007). "Calibration and data fusion solution for the miniature attitude and heading reference system." Sensors and Actuators A: Physical **138**(2): 411-420.

Koda, H., K. Sagawa, et al. (2010). "3D measurement of forearm and upper arm during throwing motion using body mounted sensor." Journal of Advanced Mechanical Design, Systems, and Manufacturing **4**(1): 167-178.

Krane, V., D. Joyce, et al. (1995). "Competitive anxiety, situation criticality, and softball performance." Sport Psychologist **8**(1): 58-72.

Kristianslund, E., T. Krosshaug, et al. (2012). "Effect of low pass filtering on joint moments from inverse dynamics: Implications for injury prevention." Journal of biomechanics **45**(4): 666-671.

Kuipers, J. B. (1999). Quaternions and rotation sequences, Princeton university press Princeton.

Lee, G. X. and K.-S. Low (2012). "A Factorized Quaternion Approach to Determine the Arm Motions Using Triaxial Accelerometers With Anatomical and Sensor Constraints." Instrumentation and Measurement, IEEE Transactions on **61**(6): 1793-1802.

Lenz, J. and A. S. Edelstein (2006). "Magnetic sensors and their applications." Sensors Journal, IEEE **6**(3): 631-649.

Limpisvasti, O., N. S. ElAttrache, et al. (2007). "Understanding Shoulder and Elbow Injuries in Baseball." Journal of the American Academy of Orthopaedic Surgeons **15**(3): 139-147.

Liu, K., T. Liu, et al. (2009). "Novel approach to ambulatory assessment of human segmental orientation on a wearable sensor system." Journal of biomechanics **42**(16): 2747.

Liu, K., W. Zhang, et al. (2009). "The development of micro-gyroscope technology." Journal of Micromechanics and Microengineering **19**(11): 113001.

Lobo, J. and J. Dias (2003). "Vision and inertial sensor cooperation using gravity as a vertical reference." Pattern Analysis and Machine Intelligence, IEEE Transactions on **25**(12): 1597-1608.

Loh, C. H., J. H. Li, et al. (2012). "Application of singular spectrum analysis to identify the degrading structure using deteriorating distributed element model." Earthquake Engineering & Structural Dynamics.

Luinge, H., P. Veltink, et al. (2007). "Ambulatory measurement of arm orientation." Journal of biomechanics **40**(1): 78-85.

Ma, Y., Z.-H. Mao, et al. (2011). "Magnetic hand tracking for human-computer interface." Magnetics, IEEE Transactions on **47**(5): 970-973.

Mayagoitia, R. E., A. V. Nene, et al. (2002). "Accelerometer and rate gyroscope measurement of kinematics: an inexpensive alternative to optical motion analysis systems." Journal of biomechanics **35**(4): 537-542.

MicroStrain. (2013). "Inertial Sensors." from http://www.microstrain.com.

Mihelj, M. (2006). "Inverse kinematics of human arm based on multisensor data integration." Journal of Intelligent and Robotic Systems **47**(2): 139-153.

MotionAnalysis. (2013). "Raptor-12 Digital RealTime System." from http://www.motionanalysis.com/html/movement/raptor12.html.

N. Marshall, R. and B. Elliott (2000). "Long-axis rotation: the missing link in proximal-to-distal segmental sequencing." Journal of sports sciences **18**(4): 247-254.

O'Donovan, K. J., R. Kamnik, et al. (2007). "An inertial and magnetic sensor based technique for joint angle measurement." Journal of biomechanics **40**(12): 2604-2611.

Oyama, S. (2012). "Baseball pitching kinematics, joint loads, and injury prevention." Journal of Sport and Health Science.

Piyabongkarn, D., R. Rajamani, et al. (2005). "The development of a MEMS gyroscope for absolute angle measurement." Control Systems Technology, IEEE Transactions on **13**(2): 185-195.

Qualisys. (2013). from http://www.qualisys.com/.

Ramadge, P. J. and W. M. Wonham (1989). "The control of discrete event systems." Proceedings of the IEEE **77**(1): 81-98.

Ren, L., R. K. Jones, et al. (2008). "Whole body inverse dynamics over a complete gait cycle based only on measured kinematics." Journal of biomechanics **41**(12): 2750-2759.

Riener, R. and A. Straube (1997). "Inverse dynamics as a tool for motion analysis: arm tracking movements in cerebellar patients." Journal of neuroscience methods **72**(1): 87-96.

Roach, N. T., M. Venkadesan, et al. (2013). "Elastic energy storage in the shoulder and the evolution of high-speed throwing in Homo." Nature **498**(7455): 483-486.

Rouhani, H., J. Favre, et al. (2011). "Ambulatory measurement of ankle kinetics for clinical applications." Journal of biomechanics **44**(15): 2712-2718.

Rouhani, H., J. Favre, et al. (2012). "Measurement of multi-segment foot joint angles during gait using a wearable system." Journal of biomechanical engineering **134**(6).

Sabatini, A. (2005). "Quaternion-based strap-down integration method for applications of inertial sensing to gait analysis." Medical and Biological Engineering and Computing **43**(1): 94-101.

Sabatini, A. M. (2006). "Quaternion-based extended Kalman filter for determining orientation by inertial and magnetic sensing." Biomedical Engineering, IEEE Transactions on **53**(7): 1346-1356.

Sagawa, K., S. Abo, et al. (2009). "Forearm Trajectory Measurement during Pitching Motion using an Elbow-mounted Sensor." Journal of Advanced Mechanical Design, Systems, and Manufacturing **3**(4): 299-311.

Schepers, H. M., H. Koopman, et al. (2007). "Ambulatory assessment of ankle and foot dynamics." Biomedical Engineering, IEEE Transactions on **54**(5): 895-902.

Schepers, H. M., D. Roetenberg, et al. (2010). "Ambulatory human motion tracking by fusion of inertial and magnetic sensing with adaptive actuation." Medical & biological engineering & computing **48**(1): 27-37.

Seroyer, S. T., S. J. Nho, et al. (2010). "The Kinetic Chain in Overhand Pitching: Its Potential Role for Performance Enhancement and Injury Prevention." Sports Health: A Multidisciplinary Approach **2**(2): 135-146.

Skog, I. and P. Händel (2006). Calibration of a MEMS inertial measurement unit. XVII IMEKO World Congress.

STMicroelectronics (2013). Technical article: Everything about STMicroelectronics' 3-axis didgital MEMS gyroscopes.

Stodden, D. F., G. S. Fleisig, et al. (2005). "Relationship of biomechanical factors to baseball pitching velocity: within pitcher variation." Journal of applied biomechanics **21**(1): 44.

Vasconcelos, J., G. Elkaim, et al. (2011). "Geometric approach to strapdown magnetometer calibration in sensor frame." Aerospace and Electronic Systems, IEEE Transactions on **47**(2): 1293-1306.

Vicon. (2013). "Vicon T-Series." from http://www.vicon.com/products.

Vinjamuri, R., D. J. Crammond, et al. (2009). "Extraction of sources of tremor in hand movements of patients with movement disorders." Information Technology in Biomedicine, IEEE Transactions on **13**(1): 49-56.

Wachowiak, M. P., G. S. Rash, et al. (2000). "Wavelet-based noise removal for biomechanical signals: a comparative study." Biomedical Engineering, IEEE Transactions on **47**(3): 360-368.

Wang, J. S., Y. L. Hsu, et al. (2010). "An inertial-measurement-unit-based pen with a trajectory reconstruction algorithm and its applications." Industrial Electronics, IEEE Transactions on **57**(10): 3508-3521.

Weinland, D., R. Ronfard, et al. (2011). "A survey of vision-based methods for action representation, segmentation and recognition." Computer Vision and Image Understanding **115**(2): 224-241.

Werner, S. L., M. Suri, et al. (2008). "Relationships between ball velocity and throwing mechanics in collegiate baseball pitchers." Journal of shoulder and elbow surgery **17**(6): 905-908.

Windolf, M., N. Götzen, et al. (2008). "Systematic accuracy and precision analysis of video motion capturing systems--exemplified on the Vicon-460 system." Journal of biomechanics **41**(12): 2776.

Xsens. (2013). from http://www.xsens.com.

Yost Engineering, I. (2013). "3-Space data-logging hand-held case." from http://www.yeitechnology.com.

Zeisig, E., M. Fahlström, et al. (2010). "A two-year sonographic follow-up after intratendinous injection therapy in patients with tennis elbow." British Journal of Sports Medicine **44**(8): 584-587.